



## **A CFD analysis of transport phenomena and electrochemical reactions in a tubular-shaped PEM fuel cell**

**Maher A.R. Sadiq Al-Baghdadi**

Fuel Cell Research Center, International Energy & Environment Foundation, Al-Najaf, P.O.Box 39, Iraq.

### **Abstract**

A fuel cell is most interesting new power source because it solves not only the environment problem but also natural resource exhaustion problem. CFD modeling and simulation for heat and mass transport in PEM fuel cells are being used extensively in researches and industrial applications to gain better understanding of the fundamental processes and to optimize fuel cell designs before building a prototype for engineering application. In this research, full three-dimensional, non-isothermal computational fluid dynamics model of a tubular-shaped proton exchange membrane (PEM) fuel cell has been developed. This comprehensive model accounts for the major transport phenomena such as convective and diffusive heat and mass transfer, electrode kinetics, transport and phase-change mechanism of water, and potential fields in a tubular-shaped PEM fuel cell. The model explains many interacting, complex electrochemical, and transport phenomena that cannot be studied experimentally. Three-dimensional results of the species profiles, temperature distribution, potential distribution, and local current density distribution are presented and analysed, with the focus on the physical insight and fundamental understanding.

**Copyright © 2013 International Energy and Environment Foundation - All rights reserved.**

**Keywords:** PEM fuel cells; Tubular; Electrochemical; Heat transfer; CFD.

### **1. Introduction**

Modelling and simulation play significant roles in fully characterizing a PEM fuel cell. Changes in operating conditions and physical parameters affecting its performance are qualitatively much better understood using CFD coding [1]. Fuel cell modelling combines multiphysics couplings ranging from electrochemistry and thermodynamics over transport phenomena in porous media to material science.

The development of physically representative models that allow reliable simulation of the processes under realistic conditions is essential to the development and optimization of fuel cells, the introduction of cheaper materials and fabrication techniques, and the design and development of novel architectures [2]. The difficult experimental environment of fuel cell systems has stimulated efforts to develop models that could simulate and predict multi-dimensional coupled transport of reactants, heat and charged species using computational fluid dynamic (CFD) methods. These models can generally be characterized by the scope of the model. In many cases, modelling efforts focus on a specific part or parts of the fuel cell, like the cathode catalyst layer [3], the cathode electrode (gas diffusion layer plus catalyst layer) [4-6], or the membrane electrode assembly (MEA) [7]. These models are very useful in that they may include a large portion of the relevant fuel cell physics while at the same time having relatively short solution times. However, these narrowly focused models neglect important parts of the fuel cell making it impossible to get a complete picture of the phenomena governing fuel cell behaviour. Models that

include all parts of a fuel cell are typically two- or three-dimensional and reflect many of the physical processes occurring within the fuel cell [8, 9]. In a real PEM fuel cell geometry, the gas diffusion layers are used to enhance the reaction area accessible by the reactants. The effect of using these diffusion layers is to allow a spatial distribution in the current density on the membrane in both the direction of bulk flow and the direction orthogonal to the flow but parallel to the membrane. This two-dimensional distribution cannot be modelled with the well-used two-dimensional models where the mass-transport limitation is absent in the third direction.

Berning and Djilali [10] used the unified approach to develop a three-dimensional model of a straight gas flow channels fuel cell. The model studied reactant concentrations, current density distributions and temperature gradients within the cell as well as water flux and species transport.

Nguyen et al. [11] developed a three-dimensional model, which accounts for mass and heat transfer, current and potential distribution within a cell using a serpentine flow field. Their results show that oxygen concentration along the gas channels decrease in the direction of flow. Also, in the gas diffusion layer, the oxygen concentration is a minimum under the land area. At high current densities the oxygen is almost completely depleted under the land areas. The result is an uneven distribution of oxygen concentration along the catalyst layer resulting in local overpotentials, which vary spatially.

Um and Wang [12] used a three-dimensional model to study the effects an interdigitated flow field. The model accounted for mass transport, electrochemical kinetics, species profiles and current density distribution within the cell. Interdigitated flow fields result in forced convection of gases, which aids in liquid water removal at the cathode. This would help improve performance at high current densities when transport limitations due to excessive water production are expected. The model shows that there is little to no difference at low to medium current densities between an interdigitated flow field and a conventional flow field. However, at higher current densities, a fuel cell with an interdigitated flow field has a limiting current, which is nearly 50% greater than an equivalent cell with a conventional flow field.

Jeon et al. [13] performed a CFD simulations for four 10 cm<sup>2</sup> serpentine flow-fields with single channel, double channel, cyclic-single channel, and symmetric-single channel patterns to investigate the effect of flow-field design. High and low inlet humidity operating conditions were studied by calculating the distributions of overpotentials, current density distribution, and membrane water content at different cell voltages. The model shows that at high inlet humidity, the double channel flow-field was predicted to have better polarization performance and uniform current density distribution, while at low inlet humidity there were little performance differences among four serpentine flow-fields. The current density profiles of cyclic-single channel and symmetric-single channel flow-fields were observed to have periodically similar plots and showed significantly low pressure drop. Considering low pressure drop of cyclic-single channel and symmetric-single channel flow-fields, these flow-fields would be advantageous for the larger scale system and low inlet humidity operation.

Choi et al. [14] used a three-dimensional CFD model to study the effects of anode flow field. In their study, hydrogen gas flow in micro-channel was numerically analyzed about various channel shapes to improve the efficiency of micro fuel cell. Flow characteristics with the same boundary condition were simulated in six different shapes of micro-channels which have been already developed and newly designed as well. The result of analysis shows that characteristics of flow such as velocity, uniformity, and flow rate, depend highly upon the channel shape itself. That means it is expectable to increase the efficiency of micro fuel cell through optimal configuration of channel shape for hydrogen gas flow.

A stepped flow field is proposed by Min [15] to improve the performance of a proton exchange membrane fuel cell. A three-dimensional model that accounts for activation polarization, ohmic polarization and concentration polarization is developed to achieve this. Numerical results demonstrate that overpotential values decrease at high current density. Generally, the concentration polarization can be ignored because of its low value. Using a stepped flow field improves the reactant concentration distribution, local current density distribution, water vapour concentration distribution and cell performance. If the number of steps approaches infinity, the stepped flow field extends to a tapered field that has the lowest cell performance. The lower the number of steps and the height of the outlet channel, the greater is the improvement in reactant diffusion to the porous layers, local current density distribution, water management and cell performance.

Virk et al. [16] presented an isothermal, three dimensional numerical analyses of a PEM fuel cell's performance with the perforated type gas flow channels. Finite element based numerical technique was used to solve this multi transport numerical model coupled with the flow in porous medium, charge balance, electrochemical kinetics and membrane water content. Numerical analyses provided a detailed

insight of the various physical phenomena, affecting this type of PEM fuel cell's performance. Results showed a better distribution of reactant species in this design of the perforated type gas distributor.

One of the new architectures in PEM fuel cell design is a tubular-shaped fuel cell. Fuel cell companies and research institutes may have carried out various systematic experimental studies for this type of the fuel cell, for different specific purposes, but most the data would be proprietary in nature and very limited data are available in the open literature. There are several reasons that make the tubular design more advantageous than the planar one for medium to high power stacks: (i) elimination of the flow field: lower pressure drop and no time-consuming machinery, (ii) uniform pressure applied to the MEA by the cathode, (iii) quicker response when switching from fuel cell mode to electrolyser mode in a unitized regenerative fuel cell, (iv) greater cathode surface that increases the amount of oxygen reduction, the rate of which is slower than the hydrogen oxidation rate. In addition, (v) tubular designs can achieve much higher active area to volume ratios, and hence higher volumetric power densities.

## 2. Model description

The present work presents a comprehensive three-dimensional, multi-phase, non-isothermal model of a PEM fuel cell that incorporates the significant physical processes and the key parameters affecting fuel cell performance. The model accounts for both gas and liquid phase in the same computational domain, and thus allows for the implementation of phase change inside the gas diffusion layers. The model includes the transport of gaseous species, liquid water, protons, and energy. Water transport inside the porous gas diffusion layer and catalyst layer is described by two physical mechanisms: viscous drag and capillary pressure forces, and is described by advection within the gas channels. Water transport across the membrane is also described by two physical mechanisms: electro-osmotic drag and diffusion. The model features an algorithm that allows for a more realistic representation of the local activation overpotentials, which leads to improved prediction of the local current density distribution. This leads to high accuracy prediction of temperature distribution in the cell. This model also takes into account convection and diffusion of different species in the channels as well as in the porous gas diffusion layer, heat transfer in the solids as well as in the gases, and electrochemical reactions. The present multi-phase model is capable of identifying important parameters for the wetting behaviour of the gas diffusion layers and can be used to identify conditions that might lead to the onset of pore plugging, which has a detrimental effect of the fuel cell performance. This model is used to analyse and evaluate the performance of a planar and a tubular-shaped PEM fuel cell.

### 2.1. Computational domain

The full computational domains for the planar and tubular-shaped PEM fuel cell consist of cathode and anode gas flow fields, and the MEA are shown in Figure 1.

### 2.2. Model equations

#### 2.2.1. Gas flow channels

In the fuel cell channels, the gas-flow field is obtained by solving the steady-state Navier-Stokes equations, i.e. the continuity equation, the mass conservation equation for each phase yields the volume fraction ( $r$ ) and along with the momentum equations the pressure distribution inside the channels. The continuity equation for the gas phase inside the channel is given by;

$$\nabla \cdot (r_g \rho_g \mathbf{u}_g) = 0 \quad (1)$$

and for the liquid phase inside the channel becomes;

$$\nabla \cdot (r_l \rho_l \mathbf{u}_l) = 0 \quad (2)$$

where  $\mathbf{u}$  is velocity vector [m/s],  $\rho$  is density [kg/m<sup>3</sup>].

Two sets of momentum equations are solved in the channels, and they share the same pressure field. Under these conditions, it can be shown that the momentum equations becomes;

$$\nabla \cdot (\rho_g \mathbf{u}_g \otimes \mathbf{u}_g - \mu_g \nabla \mathbf{u}_g) = -\nabla r_g \left( P + \frac{2}{3} \mu_g \nabla \cdot \mathbf{u}_g \right) + \nabla \cdot [\mu_g (\nabla \mathbf{u}_g)^T] \quad (3)$$

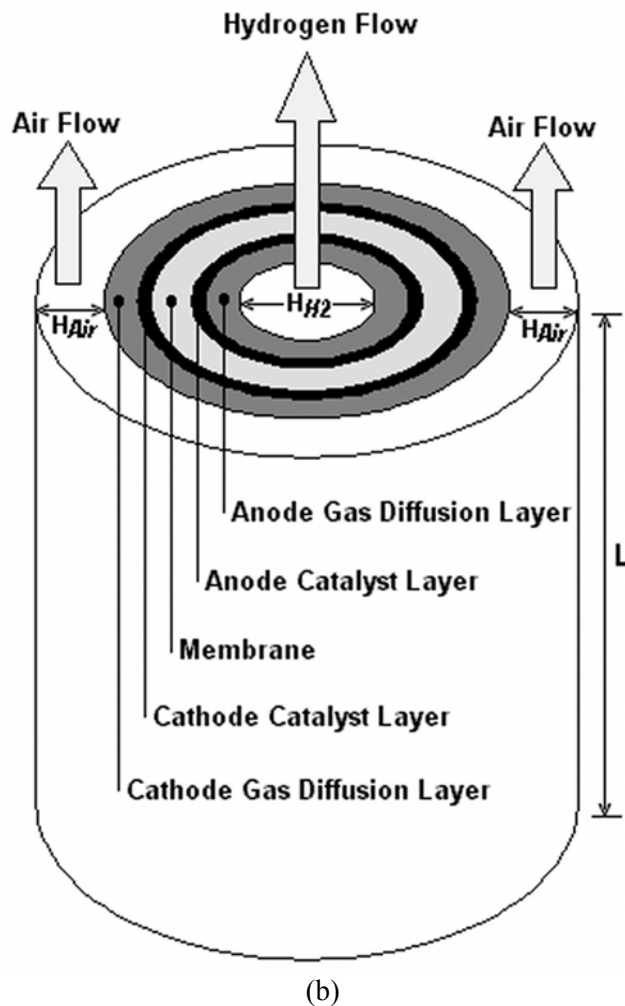
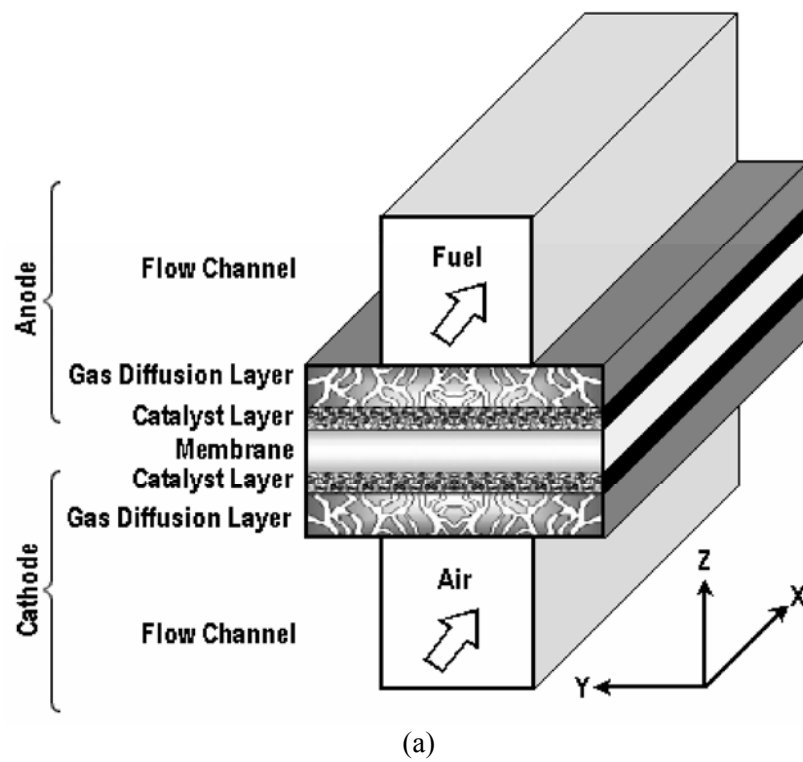


Figure 1. Three-dimensional computational domains of the planar and tubular-shaped PEM fuel cell: (a) planad and (b) tubular.

$$\nabla \cdot (\rho_l \mathbf{u}_l \otimes \mathbf{u}_l - \mu_l \nabla \mathbf{u}_l) = -\nabla r_l \left( P + \frac{2}{3} \mu_l \nabla \cdot \mathbf{u}_l \right) + \nabla \cdot [\mu_l (\nabla \mathbf{u}_l)^T] \quad (4)$$

where  $P$  is pressure (Pa),  $\mu$  is viscosity [kg/(m·s)].

The mass balance is described by the divergence of the mass flux through diffusion and convection. Multiple species are considered in the gas phase only, and the species conservation equation in multi-component, multi-phase flow can be written in the following expression for species  $i$ ;

$$\nabla \cdot \left[ \begin{array}{c} -r_g \rho_g y_i \sum_{j=1}^N D_{ij} \frac{M}{M_j} \left[ \left( \nabla y_j + y_j \frac{\nabla M}{M} \right) + (x_j - y_j) \frac{\nabla P}{P} \right] + \\ r_g \rho_g y_i \cdot \mathbf{u}_g + D_i^T \frac{\nabla T}{T} \end{array} \right] = 0 \quad (5)$$

where  $T$  is temperature (K),  $y$  is mass fraction,  $x$  is mole fraction,  $D$  is diffusion coefficient [m<sup>2</sup>/s]. Subscript  $i$  denotes oxygen at the cathode side and hydrogen at the anode side, and  $j$  is water vapour in both cases. Nitrogen is the third species at the cathode side.

The Maxwell-Stefan diffusion coefficients of any two species are dependent on temperature and pressure. They can be calculated according to the empirical relation based on kinetic gas theory [17];

$$D_{ij} = \frac{T^{1.75} \times 10^{-3}}{P \left[ \left( \sum_k V_{ki} \right)^{1/3} + \left( \sum_k V_{kj} \right)^{1/3} \right]^2} \left[ \frac{1}{M_i} + \frac{1}{M_j} \right]^{1/2} \quad (6)$$

In this equation, the pressure is in atm and the binary diffusion coefficient  $D_{ij}$  is in [cm<sup>2</sup>/s]. The values for  $(\sum V_{ki})$  are given by Fuller et al. [17].

The temperature field is obtained by solving the convective energy equation;

$$\nabla \cdot (r_g (\rho_g C_p \mathbf{u}_g T - k_g \nabla T)) = 0 \quad (7)$$

where  $C_p$  is specific heat capacity [J/(kg·K)],  $k$  is gas thermal conductivity [W/(m·K)].

The gas phase and the liquid phase are assumed to be in thermodynamic equilibrium; hence, the temperature of the liquid water is the same as the gas phase temperature.

### 2.2.2. Gas diffusion layers

The physics of multiple phases through a porous medium is further complicated here with phase change and the sources and sinks associated with the electrochemical reaction. The equations used to describe transport in the gas diffusion layers are given below. Mass transfer in the form of evaporation ( $\dot{m}_{phase} > 0$ ) and condensation ( $\dot{m}_{phase} < 0$ ) is assumed, so that the mass balance equations for both phases are;

$$\nabla \cdot ((1 - sat) \rho_g \boldsymbol{\varepsilon} \mathbf{u}_g) = \dot{m}_{phase} \quad (8)$$

$$\nabla \cdot (sat \cdot \rho_l \boldsymbol{\varepsilon} \mathbf{u}_l) = \dot{m}_{phase} \quad (9)$$

where  $sat$  is saturation,  $\varepsilon$  is porosity

The momentum equation for the gas phase reduces to Darcy's law, which is, however, based on the relative permeability for the gas phase ( $KP$ ). The relative permeability accounts for the reduction in pore space available for one phase due to the existence of the second phase [10].

The momentum equation for the gas phase inside the gas diffusion layer becomes;

$$\mathbf{u}_g = -(1 - sat) KP \cdot \nabla P / \mu_g \quad (10)$$

where  $KP$  is hydraulic permeability [m<sup>2</sup>].

Two liquid water transport mechanisms are considered; shear, which drags the liquid phase along with the gas phase in the direction of the pressure gradient, and capillary forces, which drive liquid water from

high to low saturation regions [10]. Therefore, the momentum equation for the liquid phase inside the gas diffusion layer becomes;

$$\mathbf{u}_l = -\frac{KP_l}{\mu_l} \nabla P + \frac{KP_l}{\mu_l} \frac{\partial P_c}{\partial sat} \nabla sat \quad (11)$$

where  $P_c$  is capillary pressure [Pa].

The functional variation of capillary pressure with saturation is prescribed following Leverett [10] who has shown that;

$$P_c = \tau \left( \frac{\varepsilon}{KP} \right)^{1/2} \left( 1.417(1-sat) - 2.12(1-sat)^2 + 1.263(1-sat)^3 \right) \quad (12)$$

where  $\tau$  is surface tension [N/m].

The liquid phase consists of pure water, while the gas phase has multi components. The transport of each species in the gas phase is governed by a general convection-diffusion equation in conjunction which the Stefan-Maxwell equations to account for multi species diffusion;

$$\nabla \cdot \left[ \begin{array}{l} -(1-sat)\rho_g \varepsilon y_i \sum_{j=1}^N D_{ij} \frac{M}{M_j} \left[ \left( \nabla y_j + y_j \frac{\nabla M}{M} \right) + (x_j - y_j) \frac{\nabla P}{P} \right] + \\ (1-sat)\rho_g \varepsilon y_i \cdot \mathbf{u}_g + \varepsilon D_i^T \frac{\nabla T}{T} \end{array} \right] = \dot{m}_{phase} \quad (13)$$

In order to account for geometric constraints of the porous media, the diffusivities are corrected using the Bruggemann correction formula [11];

$$D_{ij}^{eff} = D_{ij} \times \varepsilon^{1.5} \quad (14)$$

The heat transfer in the gas diffusion layers is governed by the energy equation as follows;

$$\nabla \cdot \left( (1-sat) \left( \rho_g \varepsilon C p_g \mathbf{u}_g T - k_{eff,g} \varepsilon \nabla T \right) \right) = \varepsilon \beta (T_{solid} - T) - \varepsilon \dot{m}_{phase} \Delta H_{evap} \quad (15)$$

where  $k_{eff}$  is effective electrode thermal conductivity [W/(m·K)]; the term  $[\varepsilon \beta (T_{solid} - T)]$ , on the right hand side, accounts for the heat exchange to and from the solid matrix of the GDL. The gas phase and the liquid phase are assumed to be in thermodynamic equilibrium, i.e., the liquid water and the gas phase are at the same temperature.

The potential distribution in the gas diffusion layers is governed by;

$$\nabla \cdot (\lambda_e \nabla \phi) = 0 \quad (16)$$

where  $\lambda_e$  is electrode electronic conductivity [S/m].

In order to account for the magnitude of phase change inside the GDL, expressions are required to relate the level of over- and undersaturation as well as the amount of liquid water present to the amount of water undergoing phase change. In the present work, the procedure of Berning and Djilali [10] was used to account for the magnitude of phase change inside the GDL.

### 2.2.3. Catalyst layers

The catalyst layer is treated as a thin interface, where sink and source terms for the reactants are implemented. Due to the infinitesimal thickness, the source terms are actually implemented in the last grid cell of the porous medium. At the cathode side, the sink term for oxygen is given by;

$$S_{O_2} = -\frac{M_{O_2}}{4F} i_c \quad (17)$$

where  $F$  is Faraday's constant (96487 [C/mole]),  $i_c$  is cathode local current density [A/m<sup>2</sup>],  $M$  is molecular weight [kg/mole].

Whereas the sink term for hydrogen is specified as;

$$S_{H_2} = -\frac{M_{H_2}}{2F} i_a \quad (18)$$

where  $i_a$  is anode local current density [A/m<sup>2</sup>]

The production of water is modelled as a source terms, and hence can be written as;

$$S_{H_2O} = \frac{M_{H_2O}}{2F} i_c \quad (19)$$

The generation of heat in the cell is due to entropy changes as well as irreversibility's due to the activation overpotential [2];

$$\dot{q} = \left[ \frac{T(-\Delta s)}{n_e F} + \eta_{act} \right] i \quad (20)$$

where  $\dot{q}$  is heat generation [W/m<sup>2</sup>],  $n_e$  is number of electrons transfer,  $s$  is specific entropy [J/(mole.K)],  $\eta_{act}$  is activation overpotential (V).

The local current density distribution in the catalyst layers is modelled by the Butler-Volmer equation [18, 19];

$$i_c = i_{o,c}^{ref} \left( \frac{C_{O_2}}{C_{O_2}^{ref}} \right) \left[ \exp\left( \frac{\alpha_a F}{RT} \eta_{act,c} \right) + \exp\left( -\frac{\alpha_c F}{RT} \eta_{act,c} \right) \right] \quad (21)$$

$$i_a = i_{o,a}^{ref} \left( \frac{C_{H_2}}{C_{H_2}^{ref}} \right)^{1/2} \left[ \exp\left( \frac{\alpha_a F}{RT} \eta_{act,a} \right) + \exp\left( -\frac{\alpha_c F}{RT} \eta_{act,a} \right) \right] \quad (22)$$

where  $C_{H_2}$  is local hydrogen concentration [mole/m<sup>3</sup>],  $C_{H_2}^{ref}$  is reference hydrogen concentration [mole/m<sup>3</sup>],  $C_{O_2}$  is local oxygen concentration [mole/m<sup>3</sup>],  $C_{O_2}^{ref}$  is reference oxygen concentration [mole/m<sup>3</sup>],  $i_{o,a}^{ref}$  is anode reference exchange current density,  $i_{o,c}^{ref}$  is cathode reference exchange current density,  $R$  is universal gas constant (8.314 [J/(mole.K)]),  $\alpha_a$  is charge transfer coefficient, anode side, and  $\alpha_c$  is charge transfer coefficient, cathode side.

#### 2.2.4. Membrane

The balance between the electro-osmotic drag of water from anode to cathode and back diffusion from cathode to anode yields the net water flux through the membrane;

$$N_w = n_d M_{H_2O} \frac{i}{F} - \nabla \cdot (\rho D_w \nabla c_w) \quad (23)$$

where  $N_w$  is net water flux across the membrane [kg/(m<sup>2</sup>.s)],  $n_d$  is electro-osmotic drag coefficient.

The water diffusivity in the polymer can be calculated as follow [8];

$$D_w = 1.3 \times 10^{-10} \exp \left[ 2416 \left( \frac{1}{303} - \frac{1}{T} \right) \right] \quad (24)$$

The variable  $c_w$  represents the number of water molecules per sulfonic acid group (i.e. mol  $H_2O$ /equivalent  $SO_3^{-1}$ ). The water content in the electrolyte phase is related to water vapour activity via [20];

$$\begin{aligned} c_w &= 0.043 + 17.81a - 39.85a^2 + 36.0a^3 & (0 < a \leq 1) \\ c_w &= 14.0 + 1.4(a-1) & (1 < a \leq 3) \\ c_w &= 16.8 & (a \geq 3) \end{aligned} \quad (25)$$

The water vapour activity  $a$  given by;

$$a = x_w P / P_{sat} \quad (26)$$

Heat transfer in the membrane is governed by;

$$\nabla \cdot (k_{mem} \cdot \nabla T) = 0 \quad (27)$$

where  $k_{mem}$  is membrane thermal conductivity [W/(m·K)].

The potential loss in the membrane is due to resistance to proton transport across membrane, and is governed by;

$$\nabla \cdot (\lambda_m \nabla \phi) = 0 \quad (28)$$

where  $\lambda_m$  is membrane ionic conductivity [S/m].

### 2.2.5. Potential drop across the cell

Useful work (electrical energy) is obtained from a fuel cell only when a current is drawn, but the actual cell potential, ( $E_{cell}$ ), is decreased from its equilibrium thermodynamic potential, ( $E$ ), because of irreversible losses. The various irreversible loss mechanisms which are often called overpotentials, ( $\eta$ ), are defined as the deviation of the cell potential, ( $E_{cell}$ ), from the equilibrium thermodynamic potential ( $E$ ). The cell potential ( $E_{cell}$ ) is obtained by subtracting all overpotentials ( $\eta$ ) (losses) from the equilibrium thermodynamic potential ( $E$ ) as the following expression;

$$E_{cell} = E - \eta_{act} - \eta_{ohm} - \eta_{mem} - \eta_{Diff} \quad (29)$$

The equilibrium potential is determined using the Nernst equation [21];

$$E = 1.229 - 0.83 \times 10^{-3} (T - 298.15) + 4.3085 \times 10^{-5} T \left[ \ln(P_{H_2}) + \frac{1}{2} \ln(P_{O_2}) \right] \quad (30)$$

#### 2.2.5.1. Activation Overpotential

Activation overpotential ( $\eta_{act}$ ) arises from the kinetics of charge transfer reaction across the electrode-electrolyte interface. In other words, a portion of the electrode potential is lost in driving the electron transfer reaction. Activation overpotential is directly related to the nature of the electrochemical reactions and represents the magnitude of activation energy, when the reaction propagates at the rate demanded by the current. The activation overpotential can be divided into the anode and cathode overpotentials. The anode and cathode activation overpotentials are calculated from Butler-Volmer equation (21 and 22).

#### 2.2.5.2. Ohmic Overpotential in Gas Diffusion Layers

The Ohmic overpotential ( $\eta_{ohm}$ ) is the potential loss due to current conduction through the anode and cathode gas diffusion layers, and can be modeled by equation (16).

#### 2.2.5.3. Membrane Overpotential

The membrane overpotential ( $\eta_{mem}$ ) is related to the fact that an electric field is necessary in order to maintain the motion of the hydrogen protons through the membrane. This field is provided by the existence of a potential gradient across the cell, which is directed in the opposite direction from the outer field that gives us the cell potential, and thus has to be subtracted. The overpotential in membrane is calculated from the potential equation (28).

#### 2.2.5.4. Diffusion Overpotential

Diffusion overpotential ( $\eta_{Diff}$ ) is caused by mass transfer limitations on the availability of the reactants near the electrodes. The electrode reactions require a constant supply of reactants in order to sustain the current flow. When the diffusion limitations reduce the availability of a reactant, part of the available reaction energy is used to drive the mass transfer, thus creating a corresponding loss in output voltage. Similar problems can develop if a reaction product accumulates near the electrode surface and obstructs the diffusion paths or dilutes the reactants. Mass transport loss becomes significant when the fuel cell is

operated at high current density. This is created by the concentration gradient due to the consumption of oxygen or fuel at the electrodes. The mass transport loss at the anode is negligible compared to that at the cathode. At the limiting current density, oxygen at the catalyst layer is depleted and no more current increase can be obtained from the fuel cell. This is responsible for the sharp decline in potential at high current densities. To reduce mass transport loss, the cathode is usually run at high pressure. The anode and cathode diffusion overpotentials are calculated from the following equations [2];

$$\eta_{Diff,c} = \frac{RT}{2F} \ln \left( 1 - \frac{i_c}{i_{L,c}} \right) \quad (31)$$

$$\eta_{Diff,a} = \frac{RT}{2F} \ln \left( 1 - \frac{i_a}{i_{L,a}} \right) \quad (32)$$

$$i_{L,c} = \frac{2FD_{O_2}C_{O_2}}{\delta_{GDL}} \quad (33)$$

$$i_{L,a} = \frac{2FD_{H_2}C_{H_2}}{\delta_{GDL}} \quad (34)$$

where  $i_{L,c}$  and  $i_{L,a}$  are cathode and anode local limiting current density [A/m<sup>2</sup>],  $\delta_{GDL}$  is the gas diffusion layer thickness [m], D is the diffusion coefficients [m<sup>2</sup>/s].

The diffusivity of oxygen and hydrogen are calculated from the following equations [2];

$$D_{O_2} = 3.2 \times 10^{-5} \left( \frac{T}{353} \right)^{3/2} \left( \frac{101325}{P} \right) \quad (35)$$

$$D_{H_2} = 1.1 \times 10^{-4} \left( \frac{T}{353} \right)^{3/2} \left( \frac{101325}{P} \right) \quad (36)$$

### 2.2.6. Cell power and efficiency

Once the cell potential is determined for a given current density, the output power density is found as;

$$W_{cell} = I.E_{cell} \quad (37)$$

where  $I$  is the cell operating (nominal) current density (A/m<sup>2</sup>).

The thermodynamic efficiency of the cell can be determined as [2];

$$E_{fc} = \frac{2E_{cell}F}{M_{H_2}.LHV_{H_2}} \quad (38)$$

where  $LHV_{H_2}$  is the lower heating value of hydrogen [J/kg]

## 2.3. Boundary conditions

Boundary conditions are specified at all external boundaries of the computational domain as well as boundaries for various mass and scalar equations inside the computational domain.

### 2.3.1. Inlets

The inlet values at the anode and cathode are prescribed for the velocity, temperature and species concentrations (Dirichlet boundary conditions). The inlet velocity is a function of the desired current density, the geometrical area of the membrane, the channel cross-section area, and stoichiometric flow ratio. The inlet velocities of air and fuel are calculated according to [22]:

$$u_{in,c} = \zeta_c \frac{I}{4F} A_{MEA} \frac{1}{x_{O_2,in}} \frac{RT_{in,c}}{P_c} \frac{1}{A_{ch}} \quad (39)$$

$$u_{in,a} = \zeta_a \frac{I}{2F} A_{MEA} \frac{1}{x_{H_2,in}} \frac{RT_{in,a}}{P_a} \frac{1}{A_{ch}} \quad (40)$$

where  $A_{MEA}$  is the area of the MEA [ $m^2$ ],  $A_{ch}$  is the cross sectional area of flow channel [ $m^2$ ], and  $\xi$  is the stoichiometric flow ratio.

### 2.3.2. Outlets

At the outlets of the gas-flow channels, only the pressure is being prescribed as the desired electrode pressure; for all other variables, the gradient in the flow direction is assumed to be zero (Neumann boundary conditions).

### 2.3.3. External surfaces

At the external surfaces of the cell, temperature is specified and zero heat flux is applied at the surface of the conducting boundary surfaces.

### 2.3.4. Interfaces inside the computational domain

Combinations of Dirichlet and Neumann boundary conditions are used to solve the electronic and protonic potential equations. Dirichlet boundary conditions are applied at the land area (interface between the bipolar plates and the gas diffusion layers). Neumann boundary conditions are applied at the interface between the gas channels and the gas diffusion layers to give zero potential flux into the gas channels. Similarly, the protonic potential field requires a set of potential boundary condition and zero flux boundary condition at the anode catalyst layer interface and cathode catalyst layer interface respectively.

## 2.4. Computational procedure

### 2.4.1. Computational grid

The governing equations were discretized using a finite volume method and solved using a computational fluid dynamic (CFD) code. The computational domains are divided into a finite number of control volumes (cells). All variables are stored at the centroid of each cell. Interpolation is used to express variable values at the control volume surface in terms of the control volume center values. Stringent numerical tests were performed to ensure that the solutions were independent of the grid size. A computational quadratic mesh consisting of a total of 11371 nodes and 60778 meshes for planar cell and 16927 nodes and 94547 meshes for tubular cell were found to provide sufficient spatial resolution (Figure 2). The coupled set of equations was solved iteratively, and the solution was considered to be convergent when the relative error was less than  $1.0 \times 10^{-6}$  in each field between two consecutive iterations. The calculations presented here have all been obtained on a Pentium IV PC (3 GHz, 3 GB RAM), using Windows XP operating system. The geometric and the base case operating conditions are listed in Table 1. Values of the electrochemical transport parameters for the base case operating conditions are taken from reference [23] and are listed in Table 2.

### 2.4.2. Solution algorithm

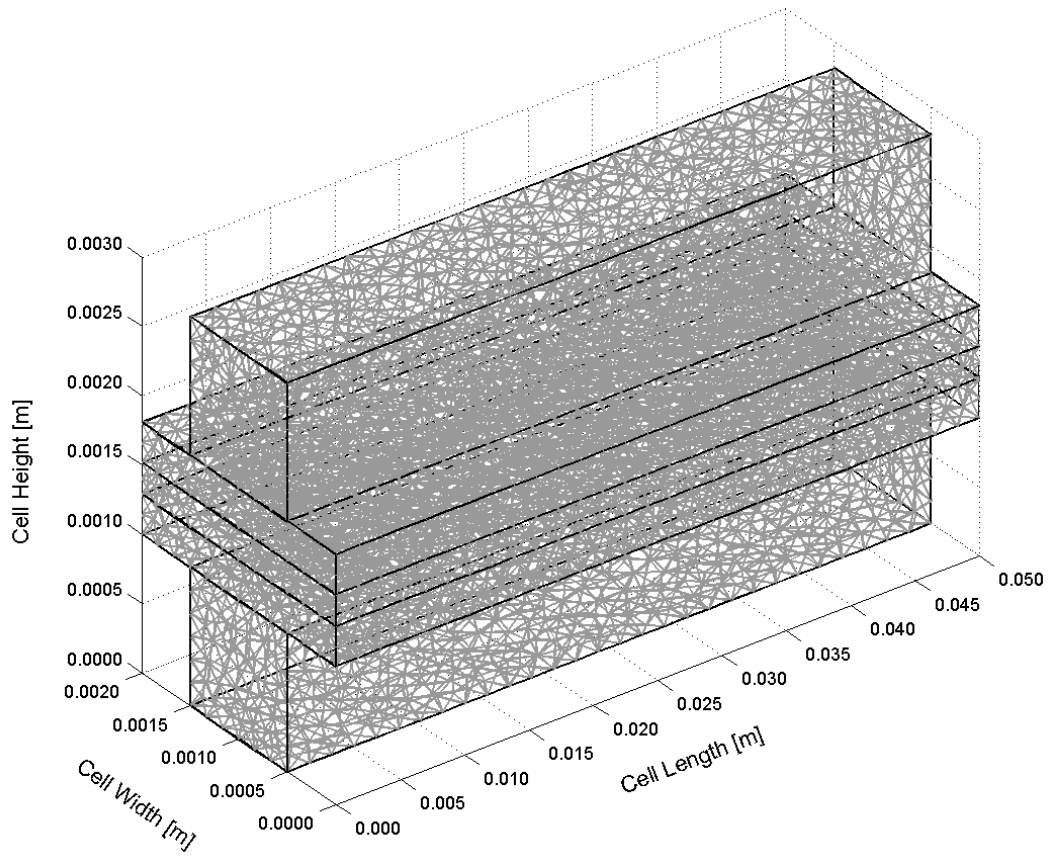
The solution begins by specifying a desired current density of the cell to be used for calculating the inlet flow rates at the anode and cathode sides. An initial guess of the activation overpotential is obtained from the desired current density using the Butler-Volmer equation. Then follows by computing the flow fields for velocities  $u, v, w$ , and pressure  $P$ . Once the flow field is obtained, the mass fraction equations are solved for the mass fractions of oxygen, hydrogen, water vapor, and nitrogen. Scalar equations are solved last in the sequence of the transport equations for the temperature field in the cell and potential fields in the gas diffusion layers and the membrane. The local current densities are solved based on the Butler-Volmer equation. After the local current densities are obtained, the local activation overpotentials can be readily calculated from the Butler-Volmer equation. The local activation overpotentials are updated after each global iterative loop. Convergence criteria are then performed on each variable and the procedure is repeated until convergence. The properties and then source terms are updated after each global iterative loop based on the new local gas composition and temperature. The strength of the current model is clearly to perform parametric studies and explore the impact of various parameters on the transport mechanisms and on fuel cell performance. The new feature of the algorithm developed in this work is its capability for accurate calculation of the local activation overpotentials, which in turn results in improved prediction of the local current density distribution. The flow diagram of the algorithm is shown in Figure 3.

Table 1. Geometrical and operational parameters for base case conditions.

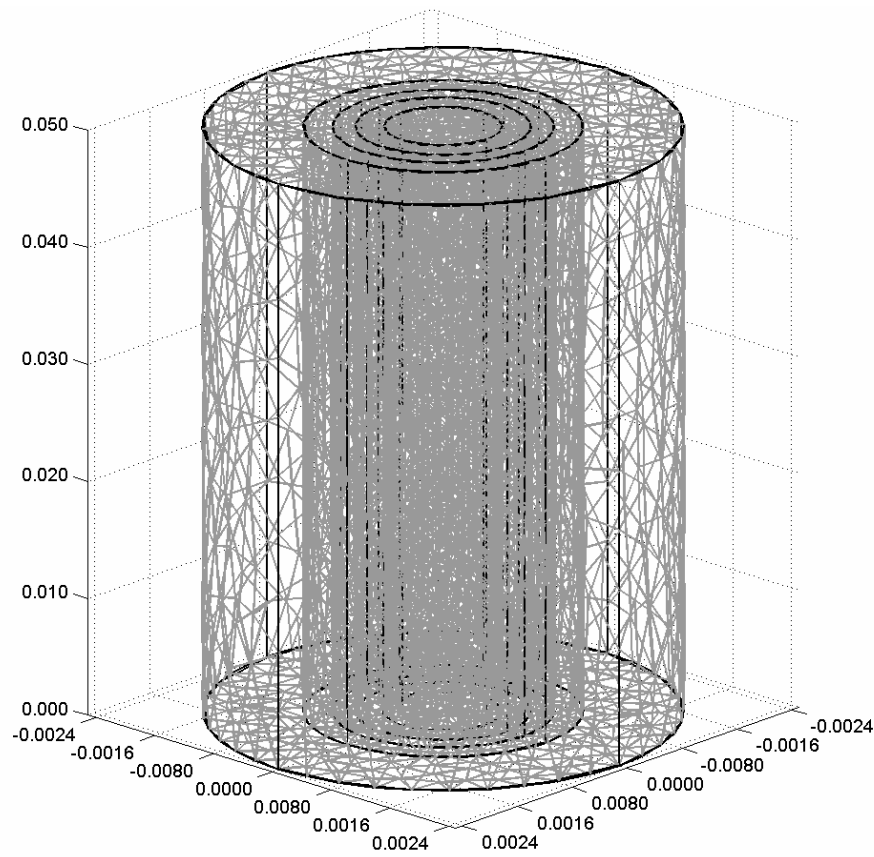
Parameter	Symbol	Value
Channel length	$L$	0.05 m
Hydrogen flow channel: diameter(tubular) / height and width(planar)	$H_{H_2}$	1e-3 m
Air flow channel: height (tubular) / height and width(planar)	$H_{Air}$	1e-3 m
Land area width	$W_{land}$	1e-3 m
Gas diffusion layer thickness	$\delta_{GDL}$	0.26e-3 m
Wet membrane thickness (Nafion® 117)	$\delta_{mem}$	0.23e-3 m
Catalyst layer thickness	$\delta_{CL}$	0.0287e-3 m
Hydrogen reference mole fraction	$x_{H_2}^{ref}$	0.84639
Oxygen reference mole fraction	$x_{O_2}^{ref}$	0.17774
Anode pressure	$P_a$	3e5 Pa
Cathode pressure	$P_c$	3e5 Pa
Inlet fuel and air temperature	$T_{cell}$	353.15 K
Relative humidity of inlet fuel and air	$\psi$	100 %
Air stoichiometric flow ratio	$\xi_c$	2
Fuel stoichiometric flow ratio	$\xi_a$	2

Table 2. Electrode and membrane parameters for base case operating conditions.

Parameter	Symbol	Value
Electrode porosity	$\varepsilon$	0.4
Electrode electronic conductivity	$\lambda_e$	100 S/m
Membrane ionic conductivity (Nafion® 117)	$\lambda_m$	17.1223 S/m
Transfer coefficient, anode side	$\alpha_a$	0.5
Transfer coefficient, cathode side	$\alpha_c$	1
Cathode reference exchange current density	$i_{o,c}^{ref}$	1.8081e-3 A/m <sup>2</sup>
Anode reference exchange current density	$i_{o,a}^{ref}$	2465.598 A/m <sup>2</sup>
Electrode thermal conductivity	$k_{eff}$	1.3 W/m.K
Membrane thermal conductivity	$k_{mem}$	0.455 W/m.K
Electrode hydraulic permeability	$kp$	1.76e-11 m <sup>2</sup>
Entropy change of cathode side reaction	$\Delta S$	-326.36 J/mol.K
Heat transfer coef. between solid and gas phase	$\beta$	4e6 W/m <sup>3</sup>
Protonic diffusion coefficient	$D_{H^+}$	4.5e-9 m <sup>2</sup> /s
Fixed-charge concentration	$c_f$	1200 mol/m <sup>3</sup>
Fixed-site charge	$z_f$	-1
Electro-osmotic drag coefficient	$n_d$	2.5
Droplet diameter	$D_{drop}$	1e-8 m
Condensation constant	$C$	1e-5
Scaling parameter for evaporation	$\varpi$	0.01



(a)



(b)

Figure 2. Computational mesh for (a) planar and (b) tubular-shaped PEM fuel cell.

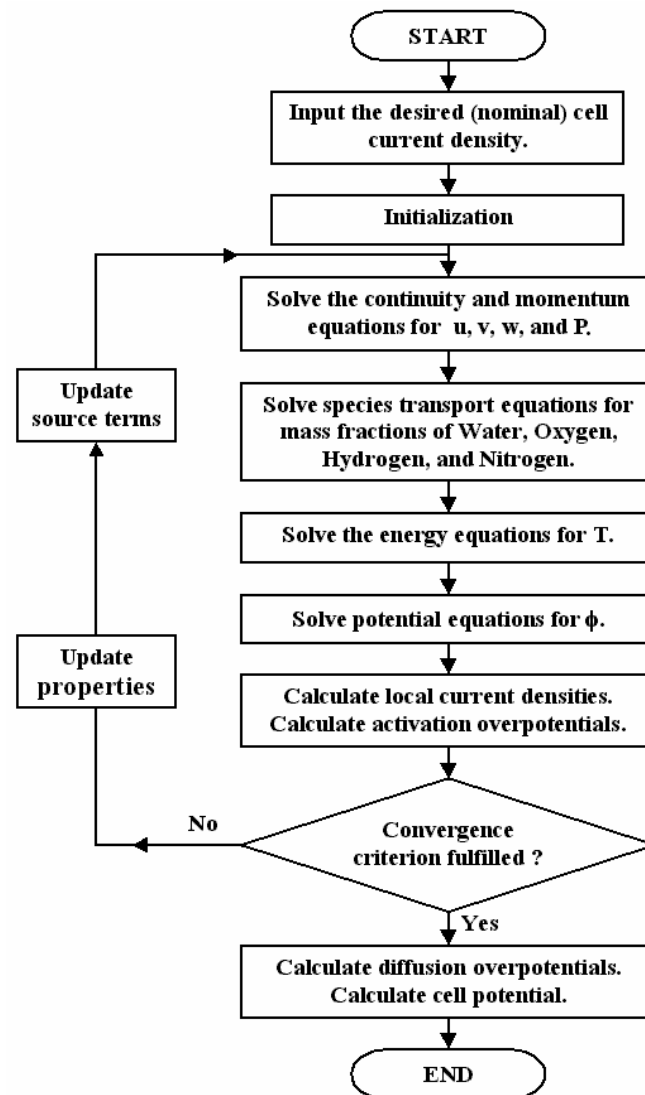


Figure 3. Flow diagram of the solution procedure used.

### 3. Results and discussion

Performance curves for planar and tubular-shaped fuel cell are shown in Figure 4 at the same operating conditions. The multi-phase model is validated by comparing model results to experimental data provided by Wang et al. [18] for the planar cell. It can be seen that the modelling results compare well with the experimental data. The importance of phase change to the accurate modelling of fuel cell performance is illustrated. By including the effects of phase change, the current model is able to more closely simulate performance, especially in the region where mass transport effects begin to dominate.

The polarization curves of the two models clearly show that higher cell potentials are achieved with the tubular design mainly because of lower activation and diffusion overpotentials. Better gas replenishment at the catalyst sites in the tubular model results in lower activation potentials. The tubular-shaped fuel cell does not seem to have higher mass transport losses. The linear behaviour of the voltage-current curve for the tubular-shaped fuel cell suggests that the overall overpotential is driven mainly by ohmic losses.

In order to gain some insight into why the polarization curve is better in the tubular-shaped PEM fuel cell, the oxygen and hydrogen distribution, local current densities, temperature distribution, and potential distribution are plotted in Figures 5-13, respectively, for a fixed nominal current density of  $1.2 \text{ A.cm}^2$ .

The detailed distribution of oxygen molar fraction for both geometries is shown in Figure 5. In the GDL of the planar shape, oxygen concentration under the land area is smaller than that under the air inlet area. The concentration of oxygen at the catalyst layer is balanced by the oxygen that is being consumed and the amount of oxygen that diffuses towards the catalyst layer driven by the concentration gradient. The lower diffusivity of the oxygen along with the low concentration of oxygen in ambient air results in

noticeable oxygen depletion under the land areas. The tubular shape gives more even distribution of the molar oxygen fraction at the catalyst layer. At a tubular shape, the oxygen mole fraction variation is low enough not to cause diffusive limitations, whereas at a planar shape the concentration of oxygen under the land areas has already reached near-zero values. The molar oxygen fraction at the catalyst layer increases with more even distribution with tubular shape. This is because of a better gas replenishment at the catalyst sites of the tubular shape results in quite uniform distribution for the oxygen to reach the catalyst layer.

Due to the relatively low diffusivity of the oxygen compared with that of the hydrogen, the cathode operation conditions usually determine the limiting current density. This is because an increase in current density corresponds to an increase in oxygen consumption.

The hydrogen molar fraction distribution in the anode side is shown in Figure 6 for both geometries. In general, the hydrogen concentration decreases from inlet to outlet as it is being consumed. However, the decrease is quite small along the channel and the decrease in molar concentration of the hydrogen under the land areas of the planar shape is smaller than for the oxygen in cathode side due to the higher diffusivity of the hydrogen.

Figure 7 shows the local current density distribution at the cathode side catalyst layer for both geometries. The local current densities have been normalized by the nominal current density in each case (i.e.  $i_c/I$ ). The local current density of the cathode side reaction depends directly on the oxygen concentration. The diffusion of the oxygen towards the catalyst layer is the main impediment for reaching high current densities. Therefore, it can be seen that for a tubular shape, the distribution of the local current density is quite uniform. This is change for planar shape, where under the land areas a noticeable decrease takes place. It can be seen that for a planar shape, a high fraction of the current is generated at the catalyst layer that lies beneath the air inlet area, leading to under-utilization of the catalyst under the land areas. This can lead to local hot spots inside the membrane electrode assembly. These hot spots can lead to a further drying out of the membrane, thus increasing the electric resistance, which in turn leads to more heat generation and can lead to a failure of the membrane. Thus, it is important to keep the current density relatively even throughout the cell. For optimal fuel cell performance, a uniform current density generation is desirable (as shown in tubular shape), and this could only be achieved with a non-uniform catalyst distribution, possibly in conjunction with non-homogeneous gas diffusion layers for planar shape.

The temperature distribution inside the fuel cell has important effects on nearly all transport phenomena, and knowledge of the magnitude of temperature increases due to irreversibilities might help prevent failure. Figure 8 shows the distribution of the temperature (in K) inside the cell for both geometries. The result of the both geometries shows that the increase in temperature can exceed several degrees Kelvin near the catalyst layer regions, where the electrochemical activity is highest. The temperature peak appears in the cathode catalyst layer, implying that major heat generation takes place in the region. In general, the temperature at the cathode side is higher than that at the anode side; this is due to the reversible and irreversible entropy production. The tubular shape design results in more even distribution of the local current density with low fraction than planer shape design. Therefore, the maximum temperature gradient appears in the planar shape design as can be seen in Figure 8. For an optimum fuel cell performance, and in order to avoid large temperature gradients inside the fuel cell, it is desirable to achieve a uniform current density distribution inside the cell.

Several transport mechanisms in the cell affect water distribution. In the membrane, primary transport is through (i) electro-osmotic drag associated with the protonic current in the electrolyte, which results in water transport from anode to cathode; and (ii) diffusion associated with water-content gradients in the membrane. One of the main difficulties in managing water in a PEM fuel cell is the conflicting requirements of the membrane and of the catalyst gas diffusion layer. On the cathode side, excessive liquid water may block or flood the pores of the catalyst layer, the gas diffusion layer or even the gas channel, thereby inhibiting or even completely blocking oxygen mass transfer. On the anode side, as water is dragged toward the cathode via electro-osmotic transport, dehumidification of the membrane may occur, resulting in deterioration of protonic conductivity. In the extreme case of complete drying, local burnout of the membrane can result.

Figure 9 shows profiles for polymer water content in the membrane for both geometries. The influence of electro-osmotic drag and back diffusion are readily apparent from this result. The tubular shape design results in more even distribution of the water content in the membrane.

Activation overpotentials (in V) distribution for both geometries is shown in Figure 10. The activation overpotential profile correlates with the local current density. For the planar shape, fresh air coming from the air inlet area has a longer distance to diffuse through to reach the land areas. This fact results in a diminished oxygen concentration at the catalyst sites under the land areas of the planar shape. Therefore, the planar shape fuel cell leads to a distribution where the maximum is located under the centre of the air inlet area and coincide with the highest reactant concentrations. Better gas replenishment at the catalyst sites in the tubular shape results in lower activation potentials with quite uniform distribution.

To perform a comprehensive comparison study for each components of the cell, two types of ohmic losses that occur in MEA are characterized. These are potential losses due to electron transport through electrodes and potential loss due to proton transport through the membrane.

Ohmic overpotential is the loss associated with resistance to electron transport in the GDLs. For a given nominal current density, the magnitude of this overpotential is dependent on the path of the electrons. The potential field (in V) in the cathodic and the anodic gas diffusion electrodes are shown in Figure 11 for both geometries. The potential distributions are normal to the flow inlet, fuel and air, and the side walls. For planar shape design, there is a gradient into the land areas where electrons flow into the bipolar plate. The distributions exhibit gradients in both x and z directions due to the non-uniform local current production and show that ohmic losses are larger in the area of the catalyst layer under the fuel and air inlet.

The potential loss in the membrane is due to resistance to proton transport across the membrane from anode catalyst layer to cathode catalyst layer. The distribution pattern of the protonic overpotential is dependent on the path travelled by the protons and the activities in the catalyst layers. Figure 12 shows the potential loss distribution (in V) in the membrane for both geometries. It can be seen that the potential drop is more uniformly distributed across the membrane for both cells. This is because of the smaller gradient of the hydrogen concentration distribution at the anode catalyst layer due to the higher diffusivity of the hydrogen.

The variation of the cathode diffusion overpotentials (in V) is shown in Figure 13 for both geometries. Tubular shape design improves the mass transport within the cell and this leads to reducing the mass transport loss. Better gas replenishment at the catalyst sites results in lower and quite uniform distribution of diffusion potentials. For planar shape design, there is a much stronger distribution of diffusion potentials at the catalyst sites, with higher values under the air inlet area. This is due to the reduction of the molar oxygen fraction at the catalyst layer under the land areas.

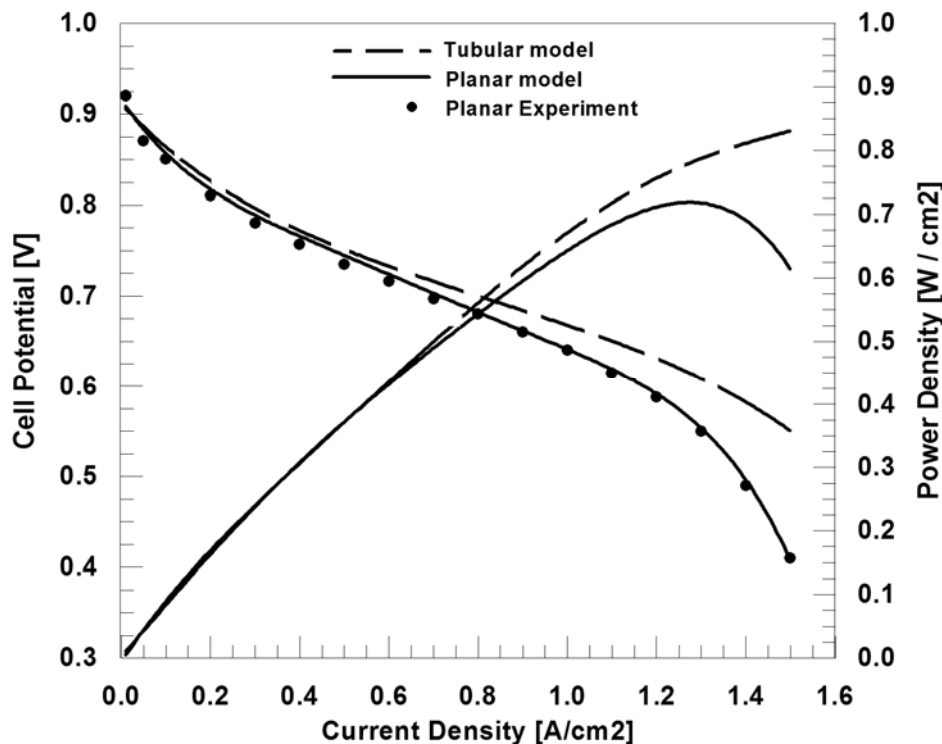
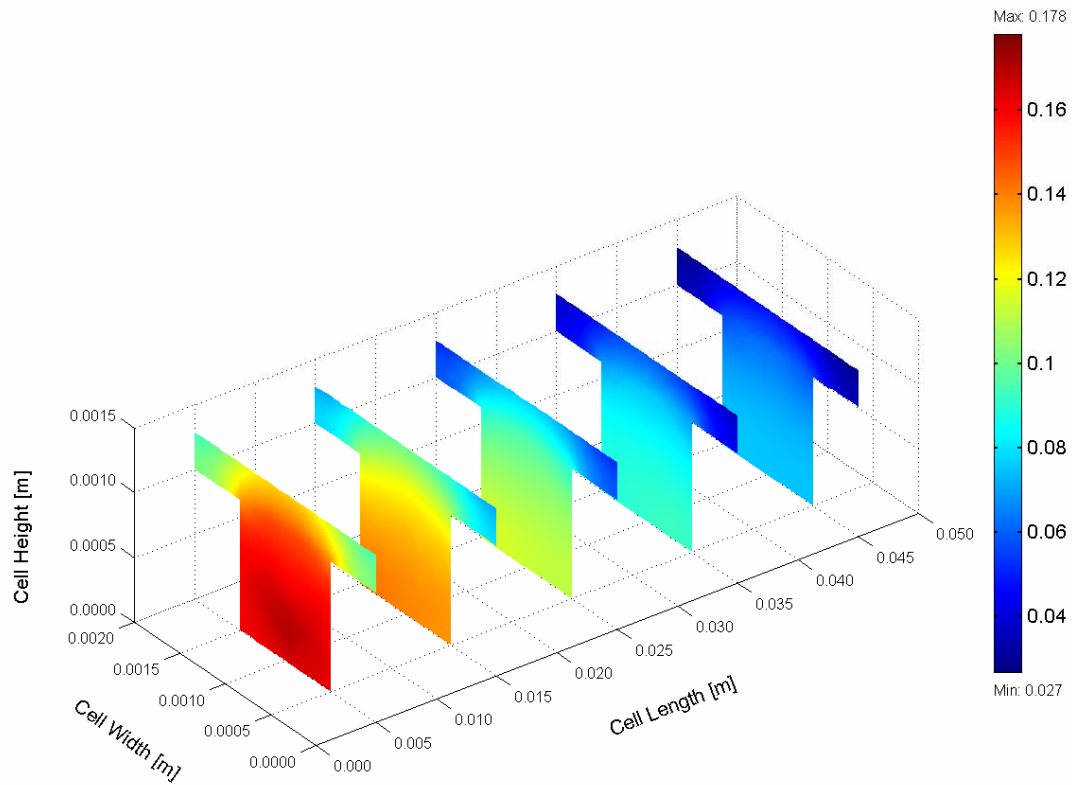
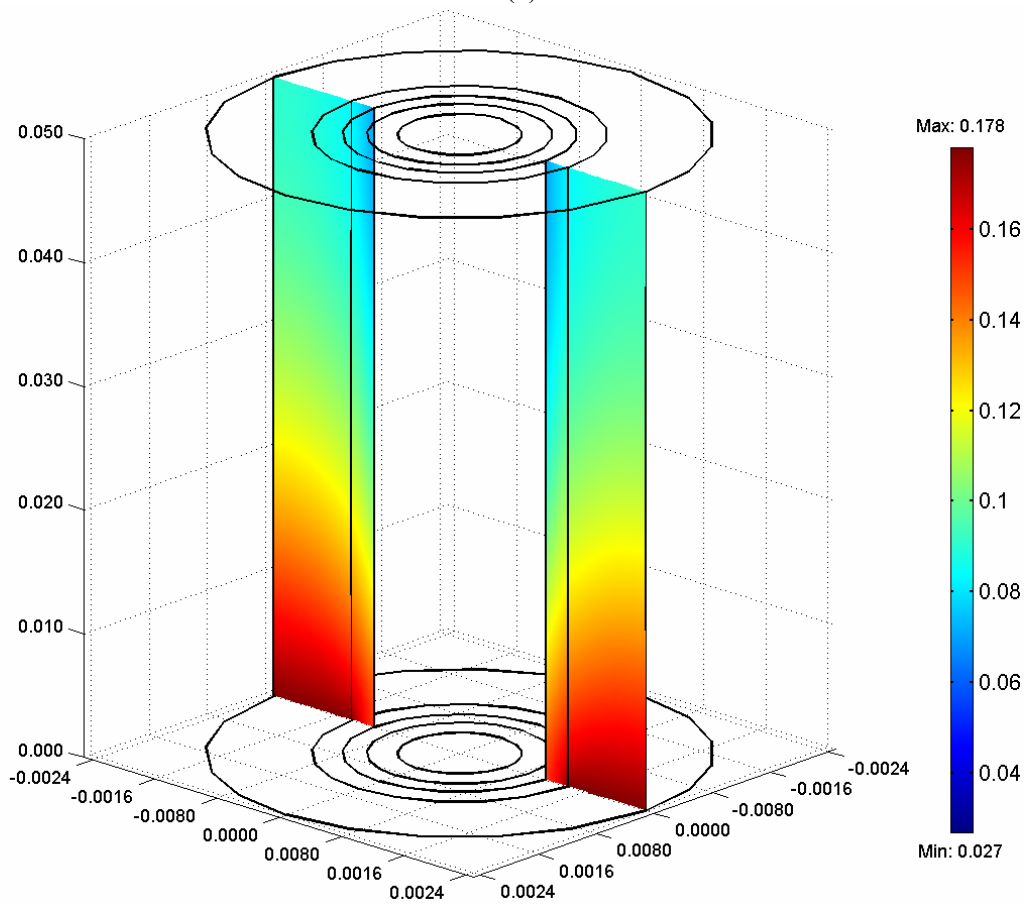


Figure 4. Comparison of the model and the experimental polarization curves.



(a)



(b)

Figure 5. Oxygen molar fraction distribution: (a) planar and (b) tubular.

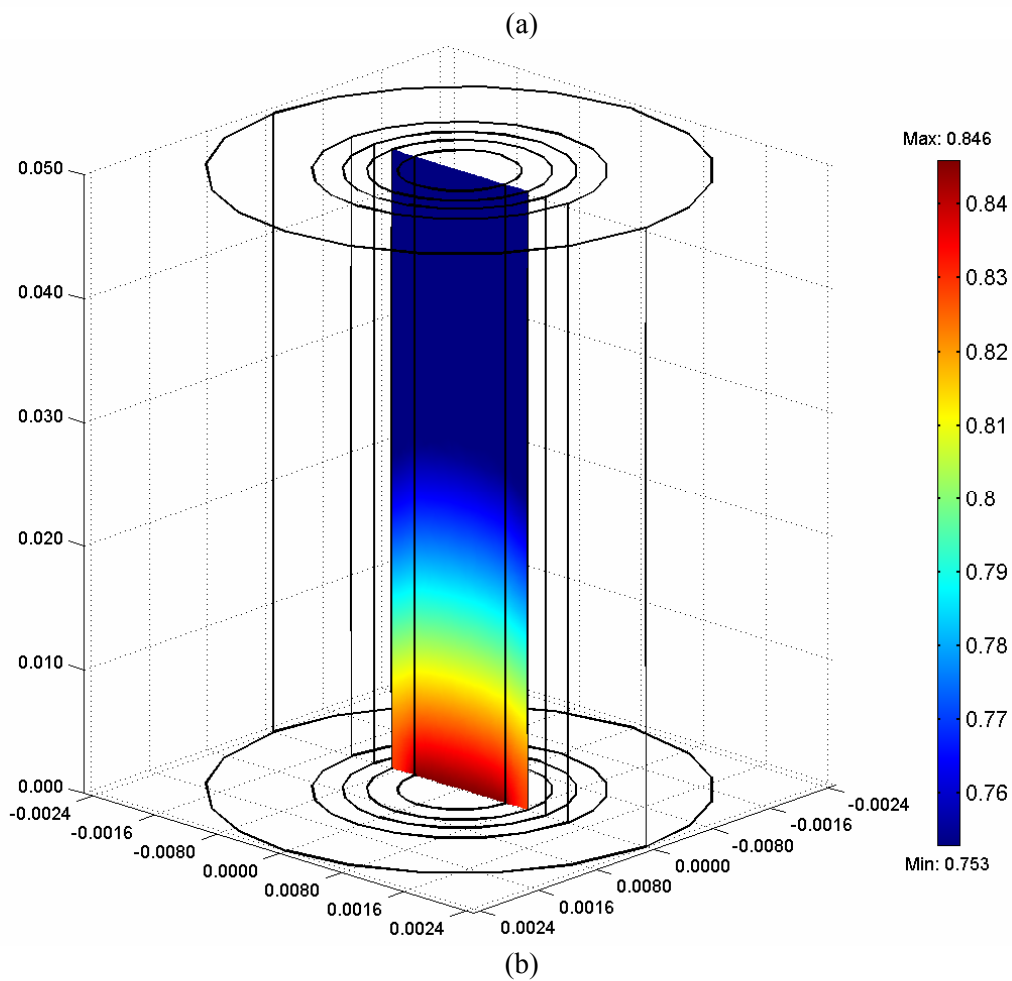
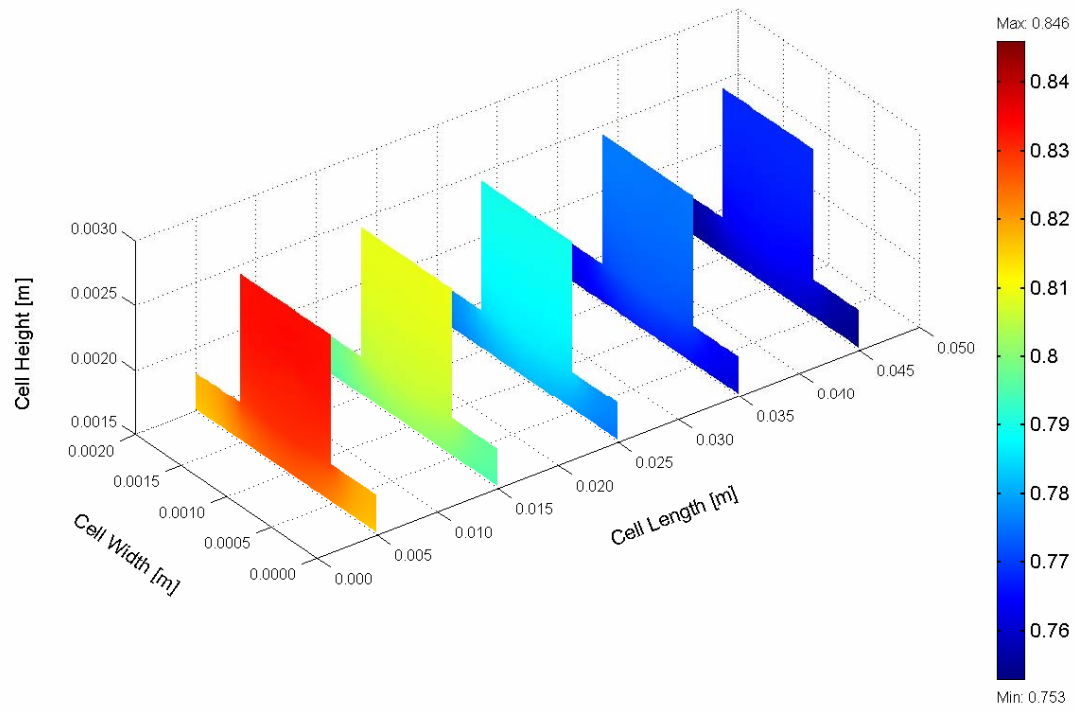


Figure 6. Hydrogen molar fraction distribution: (a) planar and (b) tubular.

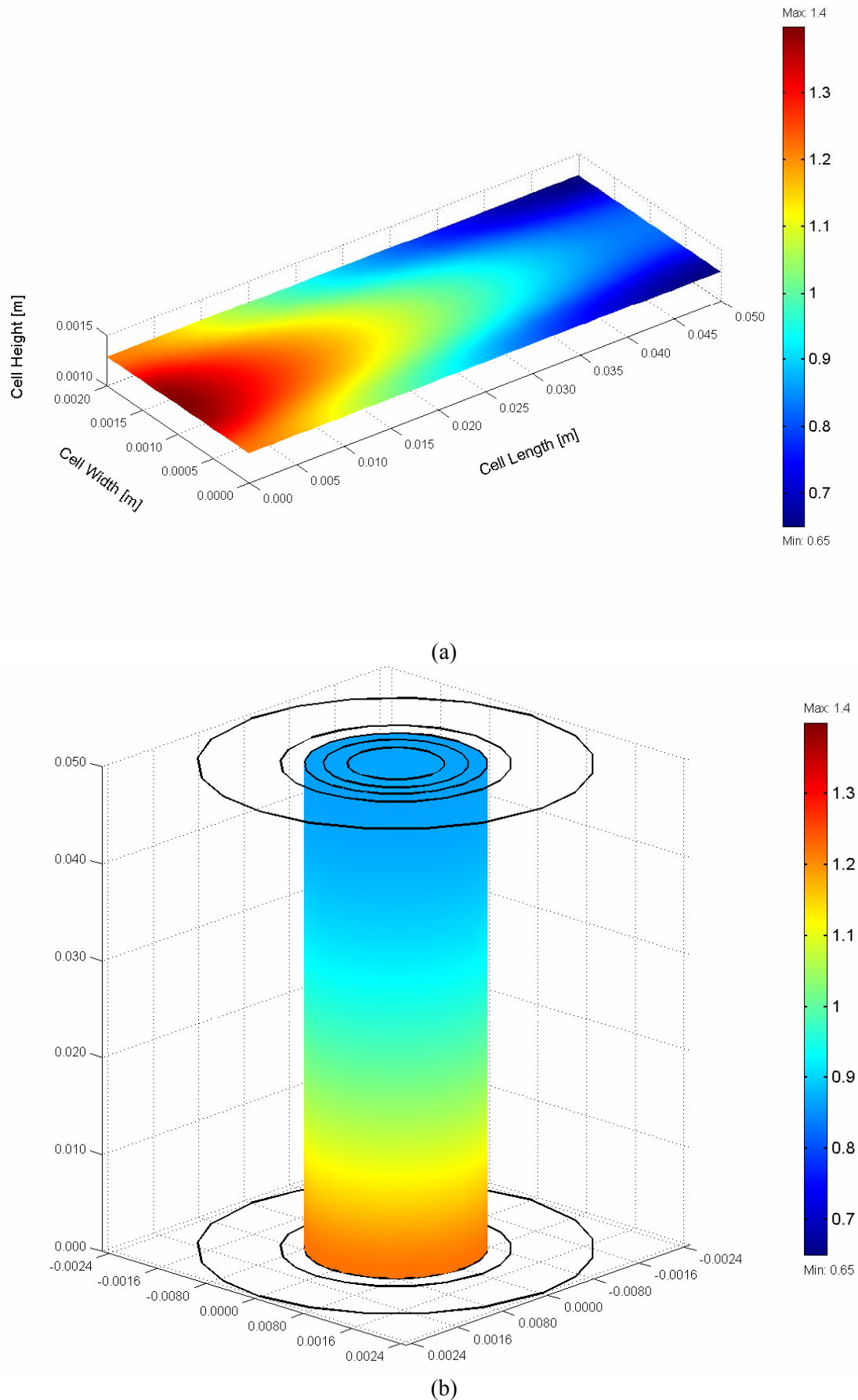
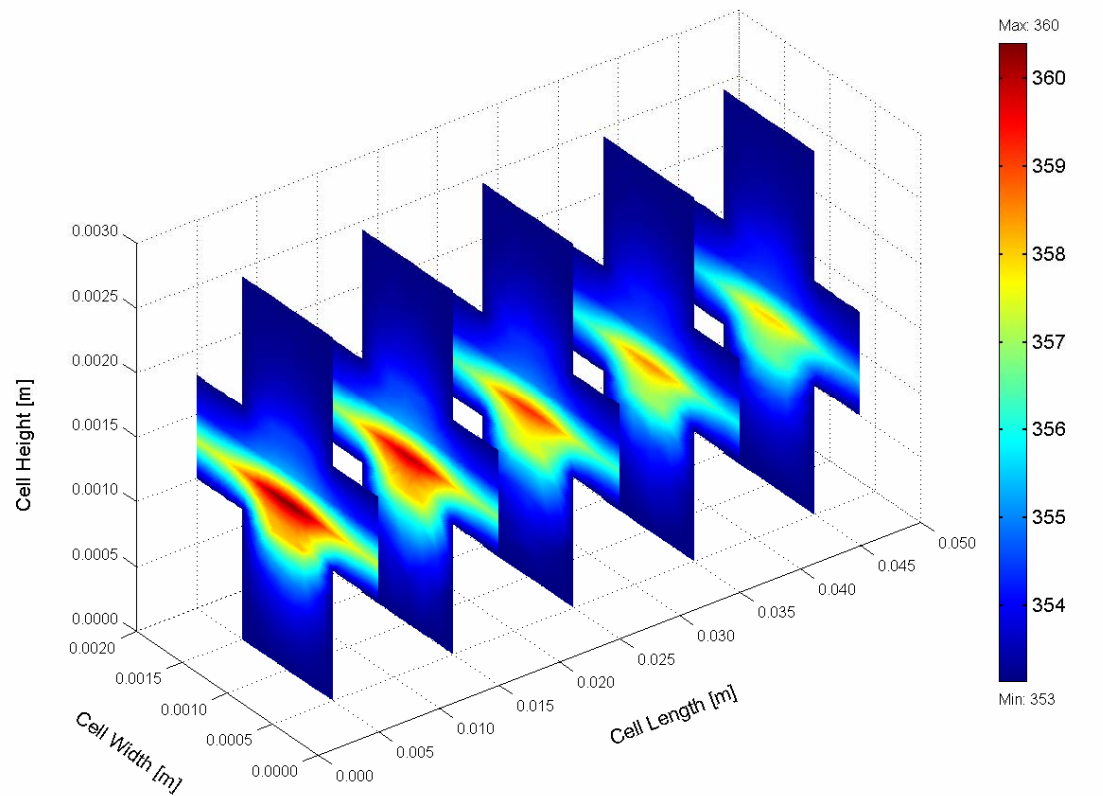
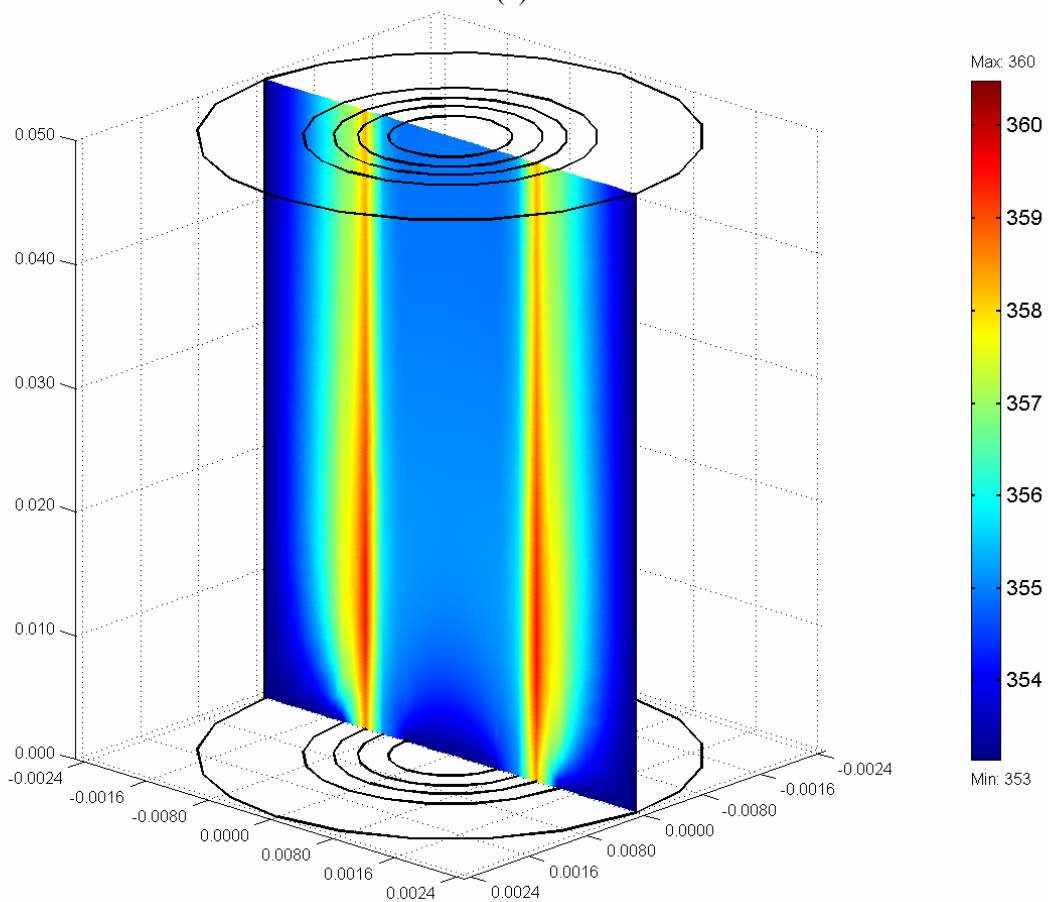


Figure 7. Dimensionless local current density distribution ( $i_c/I$ ) at cathode side catalyst layer: (a) planar and (b) tubular.

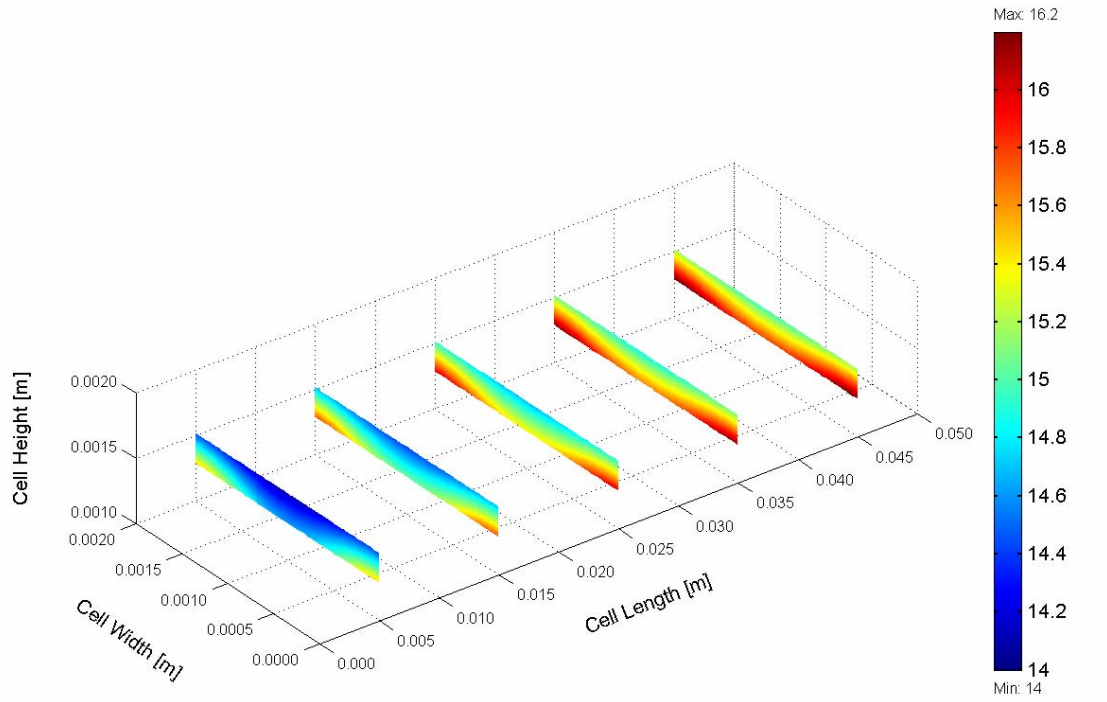


(a)

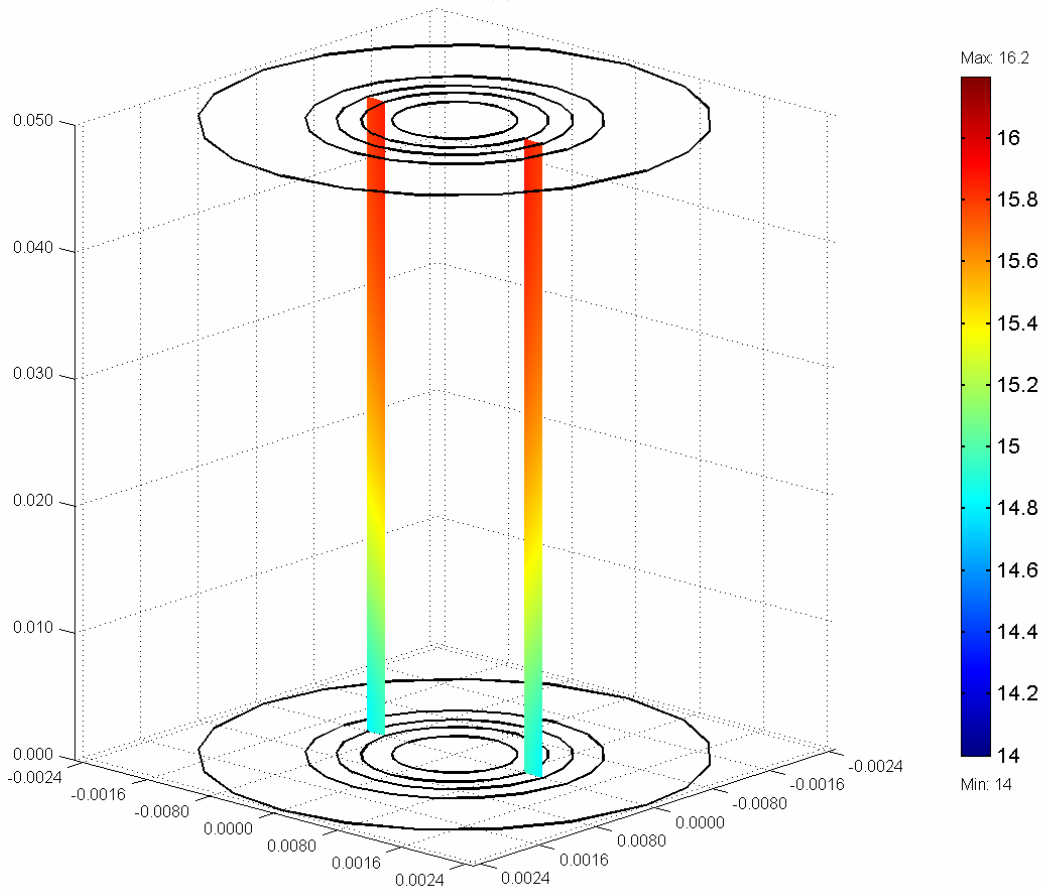


(b)

Figure 8. Temperature distribution inside the cell: (a) planar and (b) tubular.



(a)



(b)

Figure 9. Water content profiles through the MEA: (a) planar and (b) tubular.

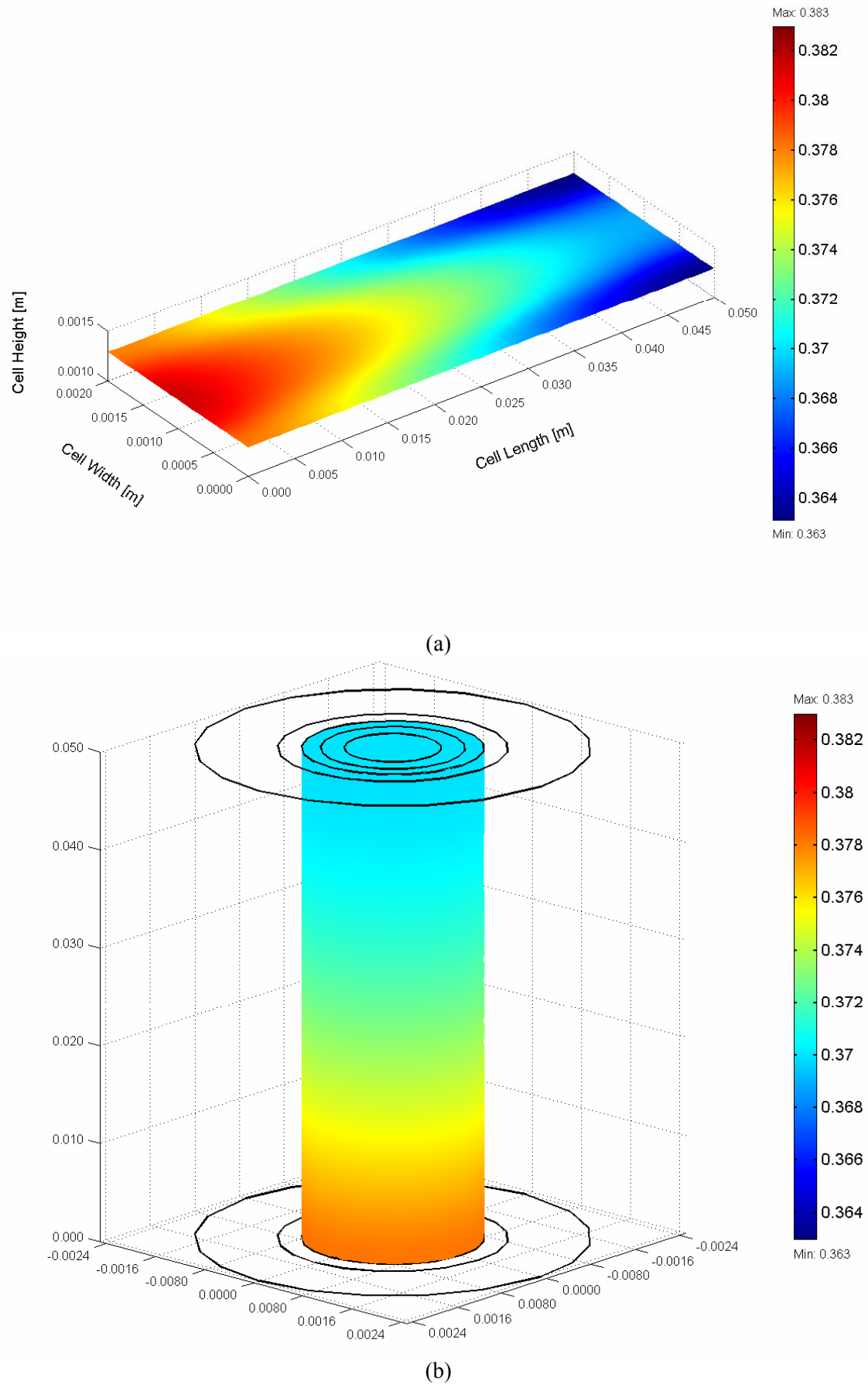
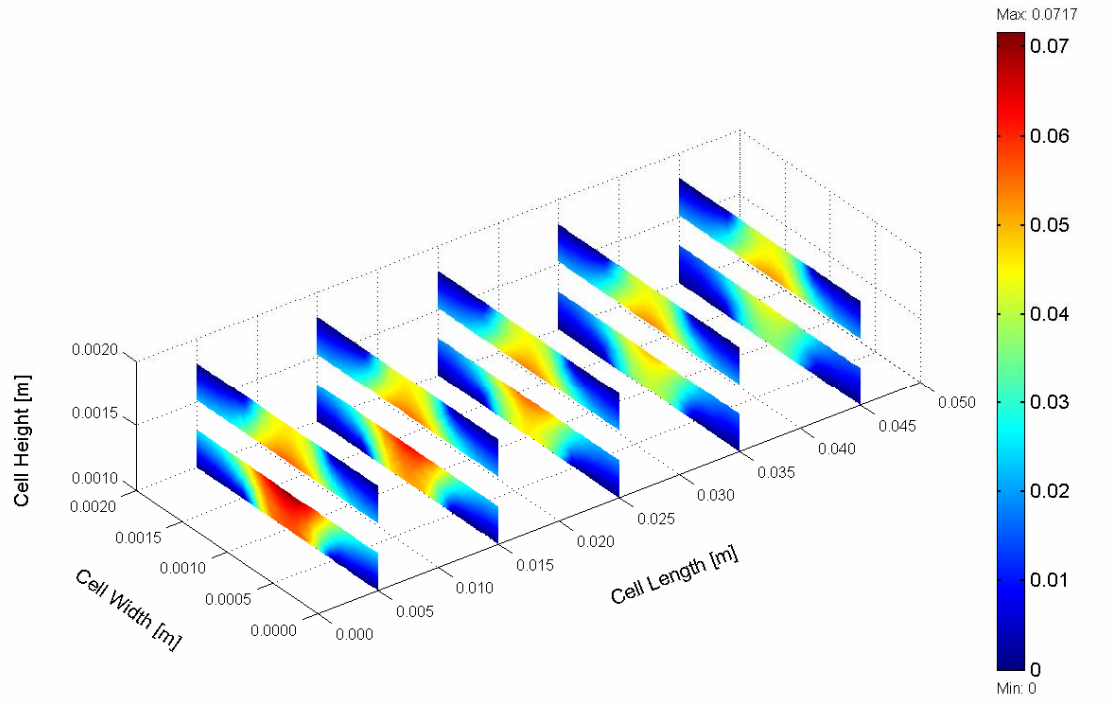
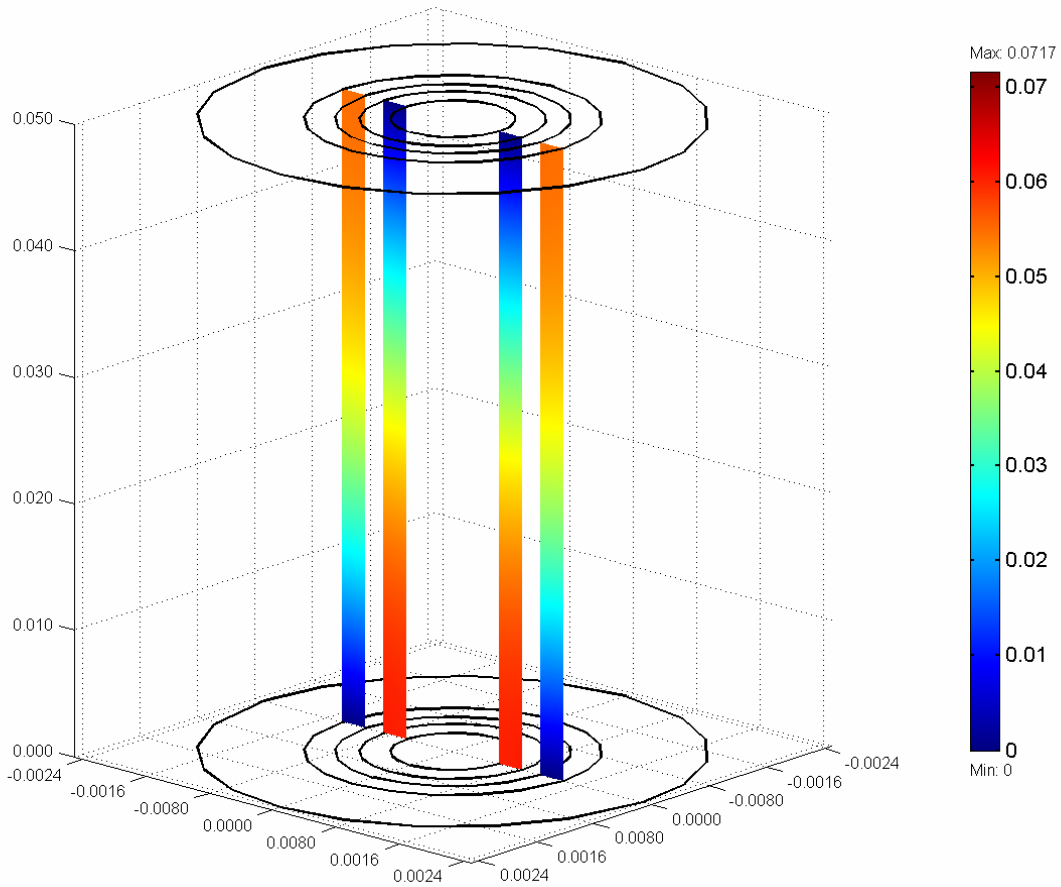


Figure 10. Activation overpotential distribution at the cathode sites: (a) planar and (b) tubular.



(a)



(b)

Figure 11. Ohmic overpotential distribution in the anode and cathode GDLs: (a) planar and (b) tubular.

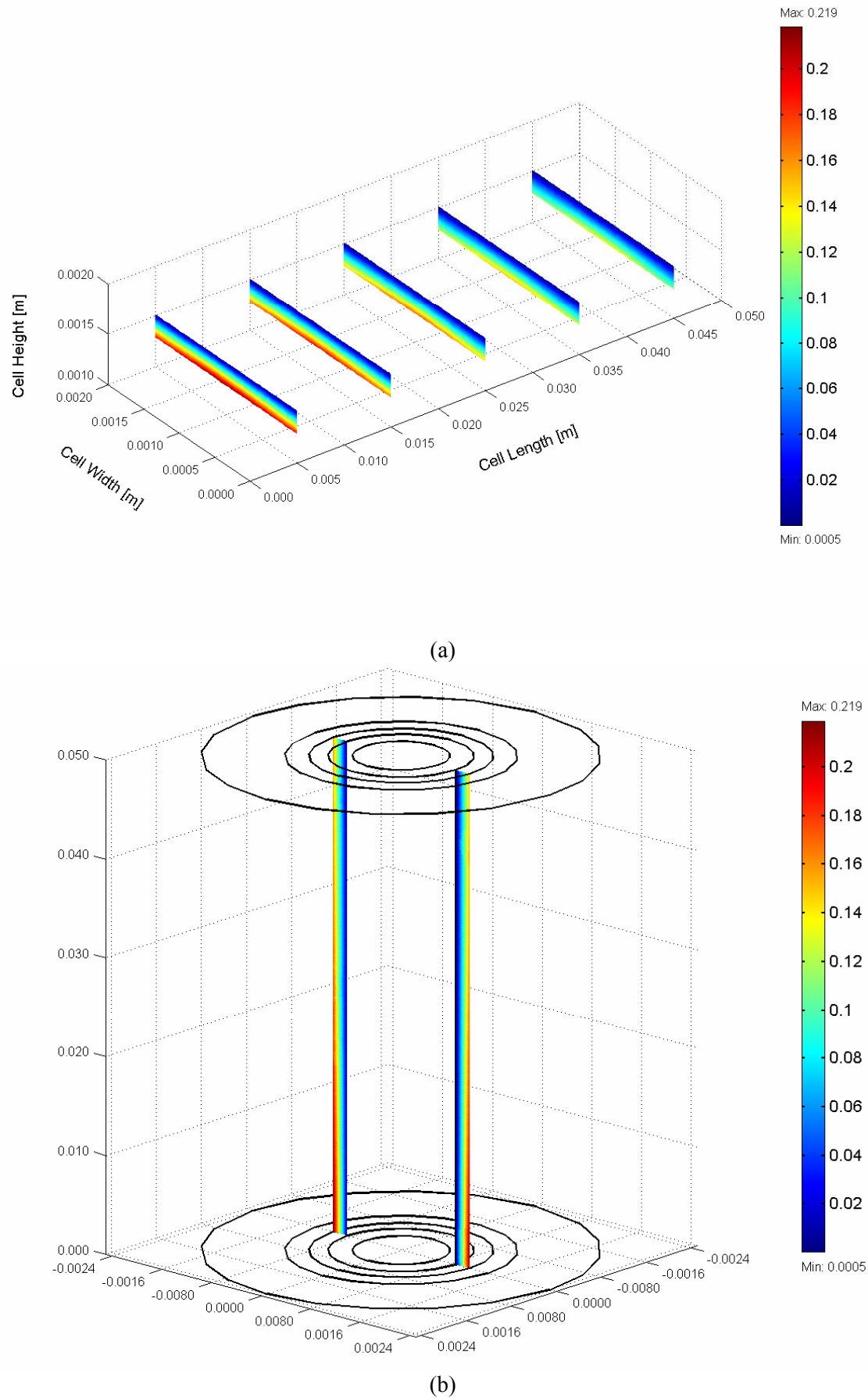


Figure 12. Membrane overpotential distribution across the membrane: (a) planar and (b) tubular.

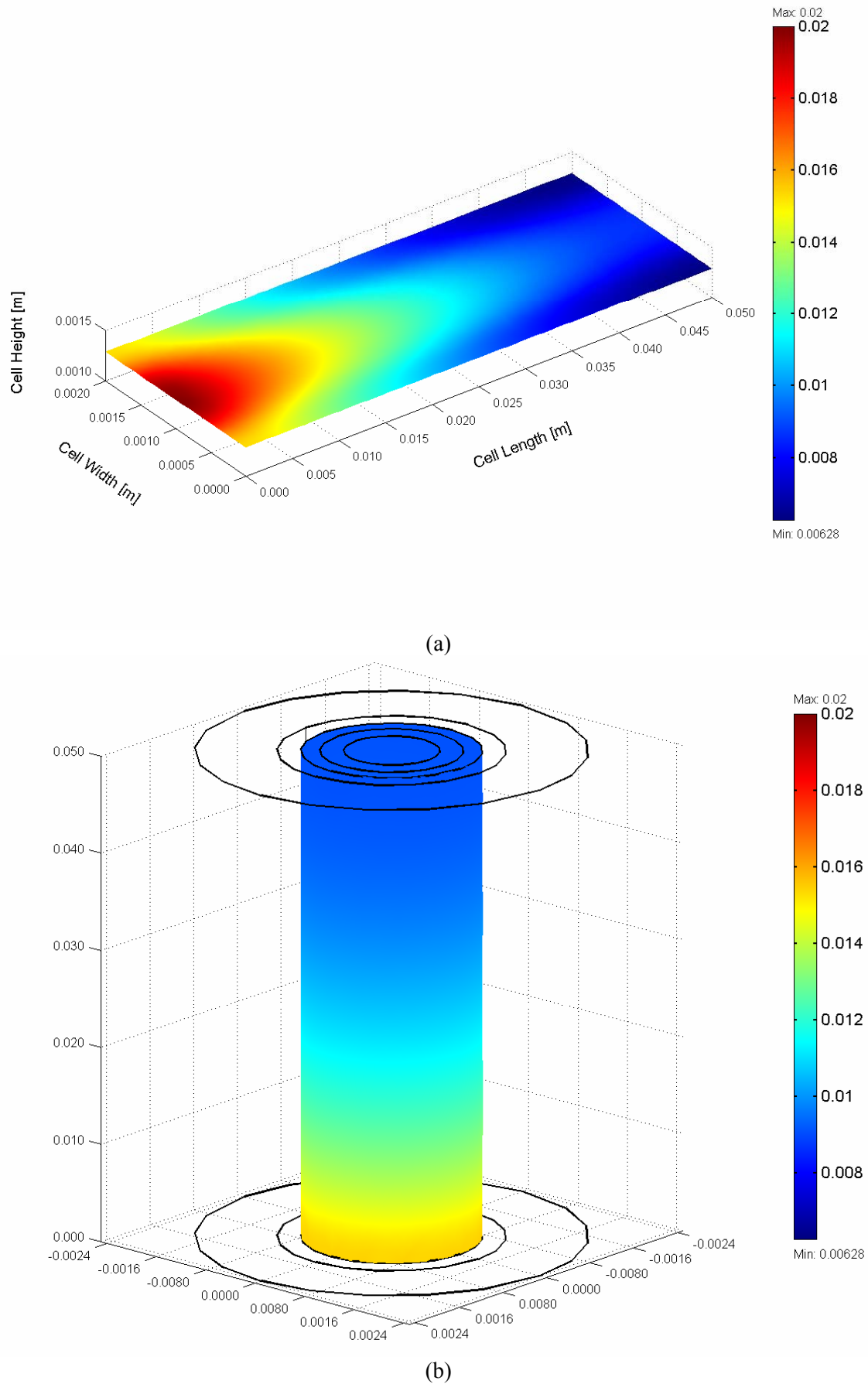


Figure 13. Diffusion overpotential distribution at the cathode sites: (a) planar and (b) tubular.

The performance of fuel cells is affected by operating point (cell voltage and related current density). Operating conditions that give optimal fuel cell performance depend on the application area. Stationary, portable, and transportation applications all have different requirements and operate in different environments. What all this means that the present 3D model can make it fast and easy to try all sorts of combinations of geometries and operating conditions to come up with an optimum design for the application. Usually, many compromises in the operating points (cell voltages and related current densities) of the specific cell are necessary to meet the application requirements, obtain lowest system cost, and achieve acceptable cell life. Operating points are based on defining specific system requirements, such as power level, voltage, efficiency, and system weight. It is necessary to select the cell operating point (cell voltage and related current density) that satisfies system requirements (such as lowest cost, lightest unit, and highest power density or such as highest efficiency and lowest operating cost). For example, a design point at high current density will allow a smaller cell size at lower capital cost to be used for the stack, but with lower system efficiency (because of the lower cell voltage) and attendant higher operating cost. This type of operating point would be typified by a portable application (such as vehicle, laptop PC, or cell phone) where light weight and small volume are important drivers for cost effectiveness. Operating at a lower current density, but higher voltage (higher efficiency, and lower operating cost) would be more suitable for stationary power plant operation. Figure 14 shows the relationship between the thermodynamic efficiency and the power density of the cell operating at base case conditions. Also, the figure shows the variation of the maximum temperature gradient inside the cell with cell power density. It is clearly shown that the efficiency at maximum power is much lower than the efficiency at partial loads, which makes the fuel cells very attractive and efficient for applications with highly variable loads where most of the time the fuel cell is operated at low load and high efficiency. The cell's nominal efficiency is therefore an arbitrary value, ranging anywhere between about 0.4 and  $\sim 0.7$ , which can be selected for any cell based on economic rather than on physical constraints. For example, for a planar cell operates at base case condition, one may select a maximum operating point at 0.56 V and 1.25 A/cm<sup>2</sup>, resulting in 0.7 W/cm<sup>2</sup> and an efficiency of 0.455 with maximum temperature gradient inside the cell of 7.9 K. However, one may get the same power output by selecting two cells, connected in series, operating at 0.733 V and 0.5 A/cm<sup>2</sup> each. Obviously, the latter would be twice as expensive, weight, and size, but it would be more efficient (0.584), and therefore would consume less fuel. Also, the latter two series cells runs with less temperature rise inside each cell (only 2.73 K), and this leads to prevent drying out of the membrane and excessive thermal stresses that may result in rupture of the membrane, and therefore less thermal management problems, and achieve long cell life.

For a tubular cell operates at base case condition, one may select a maximum operating point at 0.613 V and 1.25 A/cm<sup>2</sup>, resulting in 0.766 W/cm<sup>2</sup> and an efficiency of 0.49 with maximum temperature gradient inside the cell of 7.6 K. However, one may get the same power output by selecting two cells, connected in series, operating at 0.755 V and 0.5 A/cm<sup>2</sup> each. Obviously, the latter would be twice as expensive, weight, and size, but it would be more efficient (0.601), and therefore would consume less fuel. Also, the latter two series cells runs with less temperature rise inside each cell (only 2.69 K), and this leads to prevent drying out of the membrane and excessive thermal stresses that may result in rupture of the membrane, and therefore less thermal management problems, and achieve long cell life.

However, since efficiency drops with increasing power density, there is a trade-off between high power and high efficiency. Fuel cell designers must select the desired operating range according to whether efficiency or power is paramount for the given application.

#### 4. Conclusion

Full three-dimensional computational fluid dynamics models of planar and tubular-shaped PEM fuel cell have been developed to investigate the performance of each type. The results show that higher power densities are achieved with the tubular design mainly because of lower activation and diffusion overpotentials. Better gas replenishment at the catalyst sites in tubular design results in lower and quite uniform distribution of activation and diffusion potentials. A tubular shape evens out the local current density distribution. For a planar shape a much higher fraction of the total current is generated under the air inlet area. Therefore, the maximum temperature gradient appears in the planar shape design. The models are shown to be able to: (1) understand the many interacting, complex electrochemical and transport phenomena that cannot be studied experimentally; (2) identify limiting steps and components; and (3) provide a computer-aided tool for the design and optimization of future fuel cells to improve their lifetime with a much higher power density and lower cost. The analysis offers valuable physical insight

towards design of a cell and a cell stack, to be considered in a future study. Finally, the development of physically representative models that allow reliable simulation of the processes under realistic conditions is essential to the development and optimization of fuel cells, improve long-term performance and lifetime, the introduction of cheaper materials and fabrication techniques, and the design and development of novel architectures.

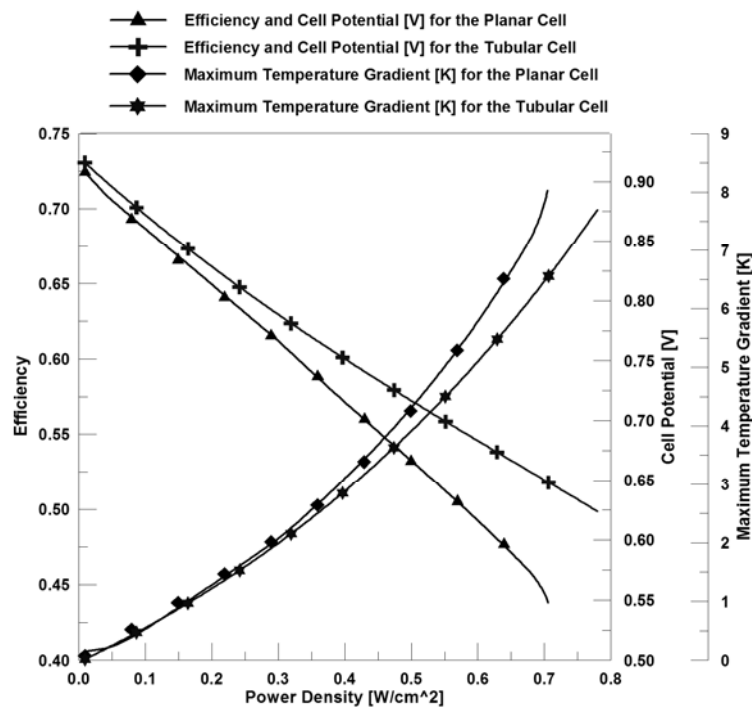


Figure 14. Relationship between the thermodynamic efficiency and the power density of the cell operates at base case conditions.

## References

- [1] F. Brèque, J. Ramousse, Y. Dubé, K. Agbossou, P. Adzakpa. *Int. Journal of Energy and Environment IJEE*, 2010; 1(1), 1-20.
- [2] Maher A.R. Sadiq Al-Baghdadi. *Int. Journal of Energy and Environment*, 2012; 3(2), 161-180.
- [3] Jeng K.T., Kuo C.P., Lee S.F. *J. Power Sources*, 2004, 128(2), 145–151.
- [4] Jaouen F., Lindbergh G., Sundholm G. *J. Electrochem. Soc.*, 2002, 149(4), A437-A447.
- [5] Grujicic M., Chittajallu K.M. *Chemical Engineering Science*, 2004, 59(24), 5883–5895.
- [6] Grujicic M., Zhao C.L., Chittajallu K.M., Ochterbeck J.M. *Materials Science and Engineering B*, 2004, 108(3), 241-252.
- [7] Francesco M. De., Arato E., Costa P. *J. Power Sources*, 2004, 132(1-2), 127–134.
- [8] Siegel N.P., Ellis M.W, Nelson D.J, Spakovsky MR.von. *J.Power Sources*, 2004, 128(2), 173-184.
- [9] Berning T., Lu D.M., Djilali N. *J. Power Sources*, 2002, 106(1-2), 284-294.
- [10] Berning T., Djilali N. *J. Electrochem. Soc.*, 2003, 150(12), A1589-A1598.
- [11] Nguyen P.T., Berning T., Djilali N. *J. Power Sources*, 2004, 130(1-2), 149-157.
- [12] Sukkee Um., Wang C.Y. *J. Power Sources*, 2004, 125(2), 40–51.
- [13] D.H.Jeon, S.Greenway, S.Shimpalee, J.W.VanZee. *Int.J. Hydrogen Energy*. 2008, 33, 1052-1066.
- [14] Injea Choi, Gisoo Shin, Kap-Seung Choi, Hyung-Man Kim. *World Electric Vehicle J.*2009, 3, 1-5.
- [15] Chun-Hua Min. *J. Power Sources*. 2009, 186, 370-376.
- [16] Muhammad S.Virk, Mohamad Y.Mustafa, Arne E.Holdo. *Int.J. Multiphysics* 2009, 3 (4), 347-360.
- [17] Fuller E.N., Schettler P.D., Giddings J.C. *Ind. Eng. Chem.*, 1966, 58(5), 18-27.
- [18] Wang L., Husar A., Zhou T., Liu H. *Int. J. Hydrogen Energy*, 2003; 28(11): 1263– 1272.
- [19] Parthasarathy A., Srinivasan S., Appleby J.A., Martin C.R. *J.Electrochem.Soc.*, 1992; 139(10): 2856-2862.
- [20] Hu M., Gu A., Wang M., Zhu X., Yu L. *Energy Conversion Manage*, 2004; 45(11-12): 1861-1882.
- [21] Maher A.R. Sadiq Al-Baghdadi. *Renewable Energy*. 2005, 30(10), 1587-1599.
- [22] Hyunchul, J.; Meng, H.; Wang, C.Y. *Int. J. Heat Mass Transfer*. 2005, 48(7), 1303–1315.
- [23] Maher A.R. Sadiq Al-Baghdadi. *Renewable Energy Journal* 2009; 34(3): 674-682.